Monthly Notices
of the
ROYAL ASTRONOMICAL SOCIETY

MNRAS **504,** 1–15 (2021)
Advance Access publication 2021 March 31

doi:10.1093/mnras/stab901

The VMC Survey – XLII. Near-infrared period–luminosity relations for RR Lyrae stars and the structure of the Large Magellanic Cloud

F. Cusano,[1]★ M. I. Moretti,[2] G. Clementini,[1] V. Ripepi,[2] M. Marconi,[2] M.-R. L. Cioni,[3] S. Rubele,[4] A. Garofalo,[1] R. de Grijs,[5,6,7] M. A. T. Groenewegen,[8] J. M. Oliveira,[9] S. Subramanian,[10] N.-C. Sun[11] and J. Th. van Loon[9]

[1]*INAF-Osservatorio di Astrofisica e Scienza dello Spazio, Via Piero Gobetti, 93/3, I-40129 Bologna, Italy*
[2]*INAF-Osservatorio Astronomico di Capodimonte, Via Moiariello 16, I-80131 Naples, Italy*
[3]*Leibniz-Institut für Astrophysik Potsdam, An der Sternwarte 16, D-14482 Potsdam, Germany*
[4]*INAF-Osservatorio Astronomico di Padova, vicolo dell'Osservatorio 5, I-35122 Padova, Italy*
[5]*Department of Physics and Astronomy, Macquarie University, Balaclava Road, Sydney, NSW 2109, Australia*
[6]*Research Centre for Astronomy, Astrophysics and Astrophotonics, Macquarie University, Balaclava Road, Sydney, NSW 2109, Australia*
[7]*International Space Science Institute–Beijing, 1 Nanertiao, Zhongguancun, Hai Dian District, Beijing 100090, China*
[8]*Koninklijke Sterrenwacht van België, Ringlaan 3, B-1180 Brussels, Belgium*
[9]*Lennard-Jones Laboratories, School of Chemical and Physical Sciences, Keele University, Staffordshire ST5 5BG, UK*
[10]*Indian Institute of Astrophysics, 2nd Block, Bangalore 560034, India*
[11]*The University of Sheffield, Western Bank, Sheffield S10 2TN, UK*

Accepted 2021 March 25. Received 2021 March 25; in original form 2020 July 23

ABSTRACT

We present results from an analysis of ∼29 000 RR Lyrae stars located in the Large Magellanic Cloud (LMC). For these objects, near-infrared time-series photometry from the VISTA survey of the Magellanic Clouds system (VMC) and optical data from the Optical Gravitational Lensing Experiment (OGLE) IV survey and the *Gaia* Data Release 2 catalogue of confirmed RR Lyrae stars were exploited. Using VMC and OGLE IV magnitudes we derived period–luminosity (*PL*), period–luminosity–metallicity (*PLZ*), period–Wesenheit (*PW*), and period–Wesenheit–metallicity (*PWZ*) relations in all available bands. More that 7000 RR Lyrae were discarded from the analysis because they appear to be overluminous with respect to the PL relations. The PL_{K_s} relation was used to derive individual distance to ∼22 000 RR Lyrae stars, and study the three-dimensional structure of the LMC. The distribution of the LMC RR Lyrae stars is ellipsoidal with the three axis $S_1 = 6.5$ kpc, $S_2 = 4.6$ kpc, and $S_3 = 3.7$ kpc, inclination $i = 22 \pm 4^\circ$ relative to the plane of the sky and position angle of the line of nodes $\theta = 167 \pm 7^\circ$ (measured from north to east). The north-eastern part of the ellipsoid is closer to us and no particular associated substructures are detected and neither any metallicity gradient.

Key words: stars: variables: RR Lyrae – galaxies: distances and redshifts – Magellanic Clouds.

1 INTRODUCTION

Among the oldest objects in the Universe ($t > 10$ Gyr) RR Lyrae stars (RRLs) are pulsating variables with low masses ($M \leq 0.85$ M$_\odot$) and helium-burning cores, which place them on the horizontal branch (HB) evolutionary sequence. RRLs are one of the most numerous type of pulsating stars, commonly found in globular clusters (GCs) and in galaxies hosting an old stellar component. The visual absolute magnitude of RRLs does not vary significantly with period, because these variables are found on the HB, but has been found and predicted to depend on metallicity according to a luminosity–metallicity relation (M_V–[Fe/H]) which is fundamental for the use of RRLs as primary distance indicators (van Albada & Baker 1971; Sandage 1981a,b). On the other hand, the dependence of the $V - K$ colour on effective temperature leads to the occurrence of a near-infrared (NIR) period–luminosity–metallicity (*PLZ*) relation for RRLs, first empirically observed by Longmore, Fernley & Jameson (1986). As comprehensively discussed by Nemec, Nemec & Lutz (1994), the effect of reddening is significantly reduced in the NIR compared with optical wavelengths ($A_{Ks}/A_V \sim 1/9$, Cardelli, Clayton & Mathis 1989) and the amplitude of pulsation is smaller than in the optical ($Amp_{Ks}/Amp_V \sim 1/4$, e.g. Braga et al. 2018), allowing the derivation of precise mean magnitudes even based on a limited number of observations. This makes the RRL *PLZ* NIR relations an even more powerful tool to measure distances than its optical counterparts. Moreover, tighter relations are derived by introducing a colour term to the *PL* relation. In particular the Wesenheit function (van den Bergh 1975; Madore 1982) includes a colour term whose coefficient is equal to the ratio of the total-to-selective extinction in a filter pair [$W(X, Y) = X - R_X \times (X - Y)$]. As such the period–Wesenheit (PW) relation is reddening-free by definition.

The Large Magellanic Cloud (LMC) is a dwarf irregular galaxy hosting several different stellar populations from old, to intermediate,

★ E-mail: felice.cusano@inaf.it

© 2021 The Author(s)
Published by Oxford University Press on behalf of Royal Astronomical Society

Downloaded from https://academic.oup.com/mnras/article/504/1/1/6206842 by INAF Capodimonte Napoli (Osservatorio Astronomico di Capodimonte (Napoli) user on 23 March 2022

to young, as well as a number of star-forming regions. It is one of the closest companions of the Milky Way and the first rung of the astronomical distance ladder. Along with the Small Magellanic Cloud (SMC), the LMC is part of the Magellanic System which also comprises the Bridge connecting the two Clouds and the Magellanic Stream. The RRLs trace the oldest stellar component and probe the structure of the LMC and SMC haloes, as opposed to Classical Cepheids (CCs), which trace regions of recent star formation like the LMC bar and spiral arms (Moretti et al. 2014).

The Magellanic RRLs have been observed in optical passbands and catalogued systematically by a number of different microlensing surveys: the Massive Compact Halo Objects survey (MACHO; Alcock et al. 1997), the Optical Gravitational Lensing Experiment (OGLE; Udalski, Kubiak & Szymanski 1997; Soszyński et al. 2016, 2019), the Experiénce pour la Recherche d'Objets Sombres 2 survey (EROS-2; Tisserand et al. 2007), and, most recently, by the *Gaia* mission (Gaia Collaboration 2016a,b, 2018a and references therein). *Gaia* is repeatedly monitoring the whole sky down to a limiting magnitude $G \sim 20.7$–21 mag. By fully mapping the Magellanic System *Gaia* is increasing the census of RRLs, revealing the whole extension of the LMC and SMC haloes as well of the Bridge region (see e.g. figs 42 and 43 of Clementini et al. 2019). About 2000 new RRLs published in the *Gaia* Data Release 2 (DR2; Clementini et al. 2019) were discovered in the Magellanic System; about 850 are outside and the remaining 1150 are inside the OGLE footprint as described by Soszyński et al. (2019). Nevertheless, the RRL catalogues published by OGLE (e.g. Soszyński et al. 2009, 2012, 2016, 2019) still represent fundamental references for the Magellanic System RRLs, since they provide light curves in the standard Johnson–Cousins V_J, I_C passbands for about 48 000 of these variables, along with their pulsation period (P), mean magnitude and amplitude in the I band, and the main Fourier parameters of their light curves.

At NIR wavelengths, an unprecedented step forward in our knowledge of the properties of the RRLs in the Magellanic System is being provided by the VISTA Y, J, K_s survey of the Magellanic Clouds system (VMC,[1] Cioni et al. 2011). The survey aims at studying the star formation history (SFH) and the three-dimensional (3D) structure of the LMC, the SMC, the Bridge and of a small section of the Magellanic Stream. The approach used to derive the SFH is based on a combination of model single-burst populations that best describes the observed colour–magnitude diagrams (CMDs; see e.g. Rubele et al. 2012, 2015, 2018). The 3D geometry, instead, is inferred from different distance indicators such as the luminosity of red clump stars (RCs; see e.g. Subramanian et al. 2017) and the NIR *PL* relations of pulsating variable stars. Results for Magellanic System pulsating stars, based on the VMC K_s-band light curves, were presented by Ripepi et al. (2012a) and Muraveva et al. (2015, 2018b) for RRLs; by Ripepi et al. (2012b, 2016, 2017) and Moretti et al. (2016) for CCs; by Ripepi et al. (2014, 2015) for anomalous and Type II Cepheids; whereas results for contact eclipsing binaries observed by the VMC were presented by Muraveva et al. (2014). A first comparative analysis of the 3D structure of the LMC and SMC, as traced by RRLs, CCs, and binaries separately, was presented by Moretti et al. (2014). In the optical a complete reconstruction of the 3D LMC was performed by Deb & Singh (2014) using RRLs and OGLE data.

NIR PL relations for RRLs in small regions of the LMC were obtained by a few authors before this paper. Szewczyk et al. (2008) obtained deep NIR J- and K-band observations of six fields near the centre of the LMC. Borissova et al. (2009) investigated the metallicity dependence of the NIR PL in the K band for 50 LMC RRLs. They found a very mild dependence of the PL relation on metallicity. Muraveva et al. (2015) presented results from the analysis of 70 RRLs located in the bar of the LMC. Combining spectroscopic metallicities and VMC K_s photometry, they derived a new NIR PLZ relation.

In this paper, we present results from an analysis of VMC Y-, J-, K_s-, and OGLE V-, I-band light curves of ∼29 000 LMC RRLs. Optical and NIR data used in this study are presented in Section 2. Section 3 describes in detail all relevant steps in our analysis to derive the *PL(Z)* and *PW(Z)* relations for the LMC RRLs. Section 4 presents the 3D structure of the LMC as traced by the RRLs. Finally, Section 5 summarizes the results and our main conclusions.

2 DATA

The observations of the VMC survey are 100 per cent complete with a total number of 110 fully completed 1.77 deg^2 VMC tiles, except for a few small gaps, of which 68 cover the LMC, 13 are located in the Bridge, 27 cover the SMC, and two are in the Stream (see fig. 1 in Cioni et al. 2017). The VMC survey was carried out with the VISTA telescope which is located at Paranal Observatory in Chile. VISTA has a primary mirror of 4.1 m diameter at whose focus is placed the VISTA InfraRed CAMera (VIRCAM) – a wide-field infrared imager. For the VMC survey the Y, J and K_s filters were used. To specifically enable the study of variable stars the survey obtained K_s photometry in time-series mode with a minimum number of 11 deep epochs (each with 750 s exposure time per tile) and two shallow epochs (each with 375 s exposure time per tile), which allow an optimal sampling of the light curves for RRLs and for CCs with periods of up to around 20–30 d, thus providing the first comprehensive multi-epoch NIR catalogue of Magellanic System variables. Further details about the properties of the VMC data obtained for variable stars can be found in Moretti et al. (2014).

The VMC images were processed by the Cambridge Astronomical Survey Unit (CASU) through the VISTA Data Flow System (VDFS) pipeline. The reduced data were then sent to the Wide Field Astronomy Unit (WFAU) in Edinburgh where the single epochs were stacked and catalogued by the Vista Science Archive (VSA; Lewis, Irwin & Bunclark 2010; Cross et al. 2012). The VMC K_s-band time-series reach a signal-to-noise ratio (S/N) of 5 at K_s ∼19.3 mag. For comparison, the IRSF Near-Infrared Magellanic Clouds Survey (Kato et al. 2007) reaches $K_s \sim 17.0$ mag for the same S/N level. The sensitivity and limiting magnitude achieved by the VMC survey allow us to obtain K_s light curves for RRLs in both Magellanic Clouds (MCs). Furthermore, the large area coverage of the VMC enables, for the first time, to systematically study the NIR *PL* relation of RRLs across the whole Magellanic System.

We cross-matched the VMC catalogue with the OGLE catalogue of RRLs in the LMC (Soszyński et al. 2016, 2019) and with the catalogue of confirmed LMC RRLs published as part of *Gaia* DR2 (Clementini et al. 2019). We used *Gaia* DR2 as the more recent eDR3 (Gaia Collaboration 2020) does not contain an updated list of variable sources. This will become available with DR3 in 2022. The total number of OGLE RRLs in the VMC footprint is ∼35 000, but in our analysis we considered only the OGLE fundamental-mode (RRab) and first-overtone pulsators (RRc): (i) for which both V and I light curves are available, (ii) without flags in the OGLE catalogue such as uncertain, secondary period, possible Anomalous Cepheid, possible δ Scuti star, etc., and (iii) with a VMC counterpart found within 1 arcsec. Our total sample thus selected included 28 132 RRLs

[1] http://star.herts.ac.uk/∼mcioni/vmc

Downloaded from https://academic.oup.com/mnras/article/504/1/1/6206842 by INAF Capodimonte Napoli (Osservatorio Astronomico di Capodimonte (Napoli) user on 23 March 2022

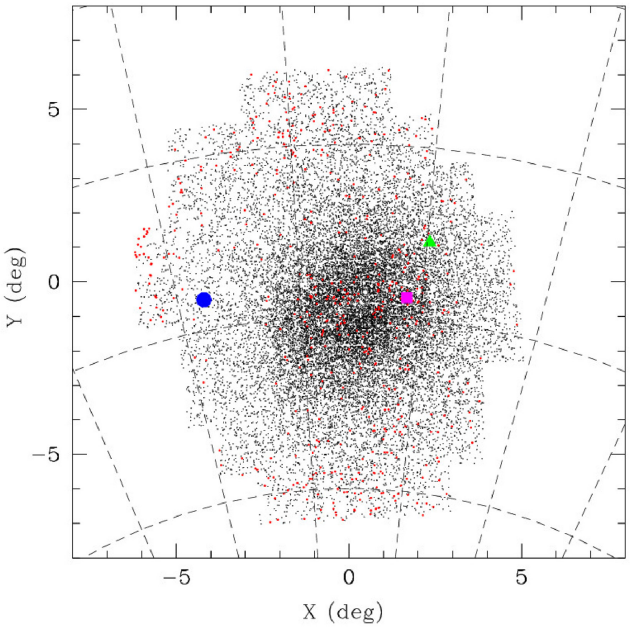

Figure 1. VMC coverage of the LMC. The black dots mark the ∼22 000 RRLs analysed in this paper. The red dots are RRLs present in the *Gaia* catalogue only. The centre of the map is $\alpha_0 = 81.0$ deg and $\delta_0 = -69.0$ deg. The blue circle, magenta square, and green triangle indicate the GCs NGC 2210, NGC 1835, and NGC 1786, respectively (see Section 4.3).

(21 152 RRab and 6980 RRc). Furthermore, we cross-matched the *Gaia* catalogue of confirmed RRLs with the general catalogue of VMC sources in the LMC field of view. This allowed us to recover an additional 524 RRLs (357 RRab, and 167 RRc) which were missing in the OGLE catalogue of LMC RRLs. *Gaia* has a smoother spatial sampling than OGLE thus allowing to recover additional RRLs in regions near to CCD edges and/or across inter-CCD gaps of the OGLE camera.

Fig. 1 shows the spatial distribution of the full sample of RRLs analysed in this work. The *X* and *Y* coordinates are defined as in van der Marel & Cioni (2001) with $\alpha_0 = 81.0$ deg and $\delta_0 = -69.0$ deg. Table 1 provides centre coordinates for the 68 VMC tiles covering the LMC and the number of RRLs contained in each tile.

Time-series *Y*, *J*, and K_s photometry for the RRLs observed by the VMC survey is provided in Table 2. The table contains the Heliocentric Julian Date (HJD) of the observations inferred from the VSA (column 1), the *Y*, *J*, and K_s magnitudes obtained using an aperture photometry diameter of 2.0 arcsec (column 2), and the error on the magnitudes (column 3). The light curves contain only epoch data observed within pre-defined constraints, that is with conditions of seeing <1 arcsec for K_s, <1.2 arcsec for *Y*, and <1.1 arcsec for *J*, airmass <1.7 and moon distance >70° (Cioni et al. 2011). The full catalogue of light curves is available in the electronic version of the paper.

The K_s photometry of the VISTA system is tied to the Two Micron All Sky Survey (2MASS; Skrutskie et al. 2006) photometry. The complete set of transformation relations from one system to the other is available on the CASU website[2] or in the work by González-Fernández et al. (2018). We used the photometry in the VISTA system v1.5. The periods provided by the OGLE catalogue were used to fold the *Y*, *J*, and K_s light curves of the RRLs observed by OGLE, whereas we used the periods provided in the *Gaia* DR2 RRL *vari*_table for the sources observed only by *Gaia* as the eDR3 release does not contain updated information for variable stars like period, epoch of maximum light, and photometry. Examples of the *Y*, *J*, and K_s light curves for an RRab and an RRc star are shown in Fig. 2. A complete atlas of light curves is provided in electronic form. The K_s light curves are very well sampled, with on average 13–14 sampling points, confirming the soundness of the VMC observing strategy for RRLs. Typical errors for the individual K_s data points are in the range of 0.06–0.1 mag. The light curves in the *Y* and *J* bands have on average four phase points. Average errors for the individual *Y* and *J* observations are 0.03 and 0.04 mag, respectively.

[2]http://casu.ast.cam.ac.uk/surveys-projects/vista/technical/photometric-properties

3 PERIOD–LUMINOSITY AND PERIOD–WESENHEIT RELATIONS

3.1 Average NIR magnitudes

Mean *Y*, *J*, and K_s magnitudes for the LMC RRLs were derived as a simple mean of magnitudes expressed in flux units, without modelling the light curves.

For RRLs observed in the optical, integrating the modelled light curve over the whole pulsation cycle is the correct procedure to derive the mean magnitude. However, in the NIR, amplitudes are so small that the difference between intensity-averaged mean magnitudes of the modelled light curves and the simple mean of the magnitudes in flux units is negligible. A comparison of the two mean values, where the former were computed by modelling the light curves with a Fourier series using the Graphical Analyzer of Time Series package (GRaTIS; custom software developed at the Bologna Observatory by P. Montegriffo, see e.g. Clementini et al. 2000), for a sample of 170 LMC RRLs showed that the differences between the two procedures are less than 0.02 mag, that is, smaller than the average errors of the two methods. Table 3 lists the *Y*, *J*, and K_s mean magnitudes obtained as simple means of the magnitudes (in flux units) along with the main properties of the stars, namely, OGLE IV or *Gaia* DR2 ID, period, pulsation mode, epoch of maximum light, VMC ID, and number of observations in the K_s, *Y*, and *J* bands.

The average magnitudes were used to place the RRLs in the $J - K_s$ versus K_s CMD, shown in Fig. 3. The RRLs are marked with small green dots. To construct the CMD we selected from the *Gaia* eDR3 catalogue (Gaia Collaboration 2020) an area of 8.8 deg in radius around the centre of the LMC ($\alpha_0 = 80.8$ deg, $\delta_0 = -69.7$ deg) which contained more than 25 million objects. We chose this area in order to fully cover the LMC regions tiled by the VMC observations as well as the whole footprint of the OGLE-IV survey. We assumed as bona fide LMC members only sources in the selected area with parallaxes (ϖ) and proper motions (μ^*_α, μ_δ) satisfying the following criterion:

$$\sqrt{((\varpi - \varpi_{\rm LMC})^2 + (\mu^*_\alpha - \mu^*_{\alpha\,\rm LMC})^2 + (\mu_\delta - \mu_{\delta\,\rm LMC})^2)} < 1, \qquad (1)$$

where $\varpi_{\rm LMC} = -0.0040 \pm 0.3346$ mas, $\mu^*_{\alpha\,\rm LMC} = 1.7608 \pm 0.4472$ mas yr^{-1}, and $\mu_{\delta\,\rm LMC} = 0.3038 \pm 0.6375$ mas yr^{-1} are the mean LMC parallax and proper motions from Gaia Collaboration (2020c). We then cross-matched the sources satisfying the above condition with the VMC general catalogue, thus obtaining a final sample of $\sim 6.9 \times 10^6$ sources shown in Fig. 3. The proper motions and parallaxes of the CMD stars are from *Gaia* eDR3 which contains the most recent and accurate astrometry and photometry available from *Gaia*.

Downloaded from https://academic.oup.com/mnras/article/504/1/1/6206842 by INAF Capodimonte Napoli (Osservatorio Astronomico di Capodimonte (Napoli) user on 23 March 2022

Table 1. VMC tiles in the LMC analysed in the present study: (1) field and tile number; (2), (3) coordinates of the tile centre, J2000 epoch; (4) total number of RRLs in the tile, (5) extinction $E(V-I)$ and (6) absorption in the K_s band (see Section 3.3); (7) average period of the RRab stars in the tile and (8) dispersion of the average period of the RRab stars (see Section 2); (9), (10), (11), (12), and (13) coefficients of the *PL* relations (in the form: $K_{s_0} = a + b \times \log P$) for RRab and fundamentalized (by adding 0.127 to the logarithm of the first overtone period) RRc stars and their uncertainties (see Section 3.4).

Tile	RA ($^h{:}^m{:}^s$)	Dec. ($^\circ{:}'{:}''$)	N	$\langle E(V-I)\rangle$ (mag)	$\langle AK_s\rangle$ (mag)	$\langle Pab\rangle$ (d)	$\sigma_{\rm Pab}$ (d)	a (mag)	b (mag)	σ_a (mag)	σ_b (mag)	rms
LMC 2_3	04:48:04	−74:54:11	84	0.121	0.035	0.577	0.067	17.45	−2.56	0.05	0.17	0.11
LMC 2_4	05:04:43	−75:04:45	111	0.134	0.039	0.586	0.061	17.50	−2.34	0.04	0.15	0.11
LMC 2_5	05:21:39	−75:10:50	125	0.158	0.046	0.575	0.066	17.44	−2.41	0.04	0.17	0.12
LMC 2_6	05:38:43	−75:12:21	107	0.128	0.037	0.596	0.082	17.38	−2.68	0.04	0.17	0.13
LMC 2_7	05:55:46	−75:09:17	82	0.145	0.042	0.577	0.066	17.43	−2.35	0.06	0.21	0.12
LMC 3_2	04:37:05	−73:14:30	114	0.105	0.031	0.594	0.064	17.46	−2.53	0.04	0.14	0.10
LMC 3_3	04:52:00	−73:28:09	170	0.111	0.032	0.587	0.069	17.43	−2.65	0.03	0.11	0.11
LMC 3_4	05:07:14	−73:37:50	216	0.127	0.037	0.580	0.063	17.45	−2.55	0.03	0.11	0.11
LMC 3_5	05:22:43	−73:43:25	250	0.121	0.035	0.589	0.072	17.42	−2.59	0.03	0.10	0.12
LMC 3_6	05:38:18	−73:44:51	218	0.133	0.038	0.578	0.064	17.42	−2.54	0.03	0.12	0.12
LMC 3_7	05:53:52	−73:42:06	160	0.115	0.033	0.579	0.082	17.45	−2.39	0.03	0.12	0.12
LMC 3_8	06:09:17	−73:35:12	138	0.118	0.034	0.573	0.059	17.38	−2.51	0.04	0.16	0.12
LMC 4_2	04:41:31	−71:49:16	232	0.139	0.040	0.581	0.062	17.46	−2.52	0.03	0.11	0.11
LMC 4_3	04:55:19	−72:01:53	311	0.110	0.032	0.584	0.068	17.45	−2.62	0.02	0.09	0.10
LMC 4_4	05:09:24	−72:10:50	485	0.080	0.023	0.578	0.067	17.47	−2.46	0.02	0.08	0.12
LMC 4_5	05:23:40	−-72:16:00	522	0.082	0.024	0.582	0.077	17.42	−2.60	0.02	0.07	0.12
LMC 4_6	05:38:00	−72:17:20	431	0.097	0.028	0.576	0.066	17.44	−2.46	0.02	0.09	0.13
LMC 4_7	05:52:20	−72:14:50	262	0.105	0.031	0.578	0.066	17.43	−2.43	0.03	0.11	0.12
LMC 4_8	06:06:33	−72:08:31	143	0.102	0.030	0.581	0.070	17.37	−2.67	0.04	0.14	0.11
LMC 4_9	06:20:33	−71:58:27	122	0.078	0.023	0.589	0.076	17.27	−2.90	0.04	0.15	0.12
LMC 5_1	04:32:44	−70:08:40	154	0.109	0.032	0.593	0.068	17.42	−2.71	0.03	0.10	0.10
LMC 5_2	04:45:19	−70:23:44	288	0.149	0.043	0.584	0.071	17.50	−2.35	0.03	0.10	0.12
LMC 5_3	04:58:12	−70:35:28	618	0.086	0.025	0.583	0.067	17.46	−2.57	0.02	0.07	0.13
LMC 5_4	05:11:17	−70:43:46	1138	0.082	0.02	0.582	0.069	17.44	−2.60	0.02	0.06	0.15
LMC 5_5	05:24:30	−70:48:34	1349	0.085	0.024	0.578	0.070	17.47	−2.42	0.02	0.06	0.16
LMC 5_6	05:37:48	−70:49:49	946	0.136	0.039	0.575	0.072	17.43	−2.52	0.02	0.08	0.17
LMC 5_7	05:51:05	−70:47:31	512	0.133	0.039	0.574	0.067	17.41	−2.53	0.02	0.09	0.14
LMC 5_8	06:04:16	−70:41:40	190	0.084	0.024	0.580	0.065	17.41	−2.48	0.03	0.10	0.11
LMC 5_9	06:17:18	−70:32:21	151	0.088	0.025	0.585	0.066	17.42	−2.43	0.03	0.12	0.10
LMC 6_1	04:36:49	−68:43:51	213	0.084	0.024	0.576	0.069	17.43	−2.59	0.03	0.11	0.13
LMC 6_2	04:48:39	−68:57:56	352	0.137	0.040	0.577	0.070	17.45	−2.54	0.03	0.09	0.13
LMC 6_3	05:00:42	−69:08:54	776	0.090	0.026	0.578	0.072	17.47	−2.53	0.02	0.08	0.17
LMC 6_4	05:12:56	−69:16:39	1305	0.094	0.027	0.581	0.074	17.47	−2.47	0.02	0.07	0.19
LMC 6_5	05:25:16	−69:21:08	1294	0.100	0.029	0.580	0.071	17.52	−2.35	0.02	0.07	0.20
LMC 6_6	05:37:40	−69:22:18	978	0.197	0.057	0.575	0.071	17.41	−2.68	0.02	0.08	0.18
LMC 6_7	05:50:03	−69:20:09	436	0.194	0.056	0.581	0.075	17.36	−2.64	0.02	0.09	0.14
LMC 6_8	06:02:21	−69:14:42	190	0.059	0.017	0.585	0.064	17.37	−2.55	0.03	0.11	0.11
LMC 6_9	06:14:33	−69:06:00	129	0.057	0.017	0.580	0.067	17.33	−2.54	0.03	0.12	0.10
LMC 6_10	06:26:32	−68:54:06	103	0.073	0.021	0.585	0.066	17.30	−2.68	0.04	0.14	0.10
LMC 7_1	04:40:09	−67:18:20	125	0.070	0.020	0.585	0.077	17.45	−2.52	0.04	0.15	0.12
LMC 7_2	04:51:35	−67:31:57	291	0.097	0.028	0.584	0.072	17.44	−2.57	0.03	0.10	0.13
LMC 7_3	05:02:55	−67:42:15	477	0.089	0.026	0.572	0.072	17.43	−2.62	0.02	0.08	0.14
LMC 7_4	05:14:24	−67:49:31	749	0.102	0.030	0.577	0.072	17.47	−2.43	0.02	0.07	0.14
LMC 7_5	05:25:58	−67:53:42	709	0.137	0.040	0.579	0.073	17.44	−2.50	0.02	0.07	0.13
LMC 7_6	05:37:35	−67:54:47	440	0.116	0.034	0.582	0.069	17.42	−2.46	0.02	0.08	0.13
LMC 7_7	05:49:12	−67:52:45	265	0.113	0.033	0.581	0.064	17.35	−2.57	0.03	0.10	0.12
LMC 7_8	06:00:45	−67:47:38	162	0.056	0.016	0.598	0.074	17.38	−2.38	0.03	0.11	0.11
LMC 7_9	06:12:12	−67:39:26	100	0.051	0.015	0.579	0.075	17.32	−2.65	0.03	0.12	0.10
LMC 7_10	06:23:29	−67:28:15	48	0.061	0.018	0.599	0.078	17.40	−2.23	0.06	0.22	0.11
LMC 8_2	04:54:12	−66:05:48	186	0.104	0.030	0.593	0.071	17.43	−2.58	0.03	0.12	0.12
LMC 8_3	05:04:54	−66:15:30	238	0.071	0.020	0.580	0.071	17.38	−2.62	0.03	0.12	0.13
LMC 8_4	05:15:43	−66:22:20	301	0.095	0.028	0.582	0.071	17.42	−2.45	0.03	0.10	0.13
LMC 8_5	05:26:38	−66:26:16	287	0.086	0.025	0.585	0.075	17.38	−2.56	0.03	0.10	0.12
LMC 8_6	05:37:34	−66:27:16	255	0.082	0.024	0.586	0.067	17.37	−2.50	0.03	0.11	0.13
LMC 8_7	05:48:30	−66:25:20	172	0.073	0.021	0.575	0.066	17.34	−2.54	0.04	0.14	0.13
LMC 8_8	05:59:23	−66:20:29	145	0.040	0.012	0.596	0.077	17.36	−2.52	0.03	0.11	0.10
LMC 8_9	06:10:11	−66:12:44	101	0.062	0.018	0.582	0.071	17.30	−2.54	0.04	0.16	0.11
LMC 9_3	05:06:41	−64:48:40	111	0.052	0.015	0.594	0.067	17.45	−2.30	0.04	0.15	0.12
LMC 9_4	05:16:55	−64:55:08	178	0.061	0.018	0.581	0.067	17.38	−2.46	0.03	0.11	0.11
LMC 9_5	05:27:14	−64:58:49	209	0.072	0.021	0.582	0.063	17.38	−2.40	0.03	0.10	0.11

Downloaded from https://academic.oup.com/mnras/article/504/1/1/6206842 by INAF Capodimonte Napoli (Osservatorio Astronomico di Capodimonte (Napoli) user on 23 March 2022

Table 1 – *continued*

Tile	RA ($^h.^m.^s$)	Dec. ($^\circ.'.''$)	N	$\langle E(V-I)\rangle$ (mag)	$\langle AK_s\rangle$ (mag)	$\langle Pab\rangle$ (d)	$\sigma_{\rm Pab}$ (d)	a (mag)	b (mag)	σ_a (mag)	σ_b (mag)	rms
LMC 9_6	05:37:35	−64:59:44	163	0.059	0.017	0.582	0.063	17.28	−2.67	0.03	0.12	0.11
LMC 9_7	05:47:55	−64:57:53	117	0.068	0.020	0.589	0.065	17.35	−2.37	0.04	0.14	0.11
LMC 9_8	05:58:13	−64:53:15	114	0.047	0.014	0.588	0.071	17.31	−2.49	0.04	0.14	0.10
LMC 9_9	06:08:26	−64:45:53	61	0.083	0.024	0.568	0.062	17.23	−2.81	0.06	0.20	0.12
LMC 10_4	05:18:01	−63:27:54	107	0.045	0.013	0.583	0.070	17.37	−2.49	0.03	0.12	0.09
LMC 10_5	05:27:49	−63:31:23	116	0.061	0.018	0.587	0.065	17.33	−2.59	0.04	0.14	0.11
LMC 10_6	05:37:38	−63:32:13	105	0.077	0.022	0.585	0.066	17.36	−2.38	0.04	0.14	0.11
LMC 10_7	05:47:26	−63:30:25	91	0.050	0.015	0.581	0.070	17.32	−2.53	0.05	0.19	0.12

Table 2. Y, J, and K_s time-series photometry for the RRLs analysed in this paper. The table is published in its entirety as Supporting Information with the electronic version of the article. A portion is shown here for guidance regarding its format and content.

VMC-558396536162		
HJD−2400000	Y	err_Y
55583.680443	18.24	0.02
55597.606813	18.42	0.03
55878.818319	18.39	0.03
55983.600130	18.30	0.02
56004.513472	18.51	0.03
HJD−2400000	J	err_J
55589.666983	18.07	0.02
55615.569205	18.13	0.03
55980.563227	18.10	0.03
56004.533138	18.22	0.04
HJD−2400000	K_s	err_{Ks}
55979.576519	17.73	0.05
55980.586298	17.78	0.08
55981.562849	17.71	0.05
55983.620398	17.78	0.07
55986.562678	17.83	0.06
55992.575373	17.80	0.07
56009.519064	17.76	0.07
56178.854539	17.78	0.05
56197.794262	17.86	0.06
56214.835096	17.89	0.06
56232.750233	17.77	0.05
56232.792530	17.76	0.05
56255.668172	17.89	0.06
57044.537788	18.05	0.13

3.2 Reddening from the RRLs

For each RRL pulsating in the fundamental mode a reddening estimate was obtained using the relation derived by Piersimoni, Bono & Ripepi (2002), which provides the intrinsic $V-I$ colour of fundamental-mode RRLs as a function of the star's period and amplitude in the V band:

$$(V-I)_0 = 0.65(\pm0.02) - 0.07(\pm0.01)\mathrm{AmpV} + 0.36(\pm0.06)\log P \quad \sigma = 0.02, \tag{2}$$

where periods and amplitudes (in the I band) for the RRLs were taken from the OGLE IV catalogue (Soszyński et al. 2016), and the I-band amplitudes were transformed to V-band amplitudes by adopting a fixed amplitude scaling factor of AmpV/AmpI=1.58. This value was derived from a statistically significant (75) data set of RRLs

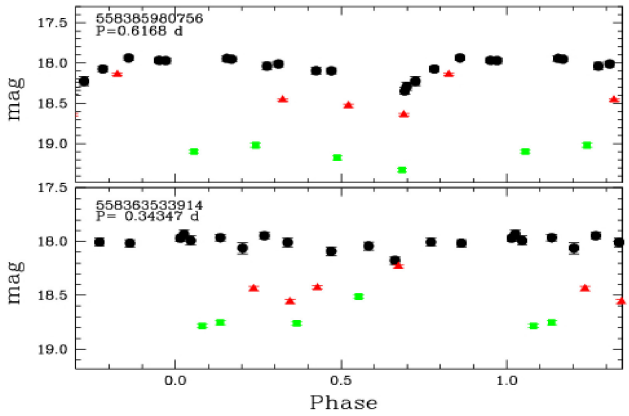

Figure 2. Y (green squares), J (red triangles), and K_s (black dots) light curves for an RRab (top panel) and an RRc (bottom panel) star in the LMC field. The VMC ID and the period are provided in the top left-hand corner. Typical errors for individual K_s epochs are about 0.06 and 0.1 mag for RRab and RRc stars, respectively. For Y- and J-bands typical errors are 0.03 and 0.07 mag for RRab and RRc stars, respectively.

in Galactic GCs (see Di Criscienzo et al. 2011). The intrinsic $V-I$ colours were then used to derive individual $E(V-I)$ reddening values for each RRL. These $E(V-I)$ values were then converted to extinction in the Y, J, and K_s passbands using the coefficients: $A_Y = 0.385\mathrm{A}_V$, $A_J = 0.283A_V$, and $A_K = 0.114\mathrm{A}_V$ with $A_V = 2.4E(V-I)$ from Kerber et al. (2009), which were derived from the Cardelli et al. (1989) extinction curve. The RRL absorption map in the K_s band derived from the RRab stars is shown in Fig. 4. This map was used to estimate by interpolation the absorption for the RRLs in the *Gaia* sample which lack V and I magnitudes and for the RRc stars for which equation (2) is not applicable. The complete set of A_{K_s} values is given in the ninth column of Table 3. It is interesting to note how the most active star-forming regions in the LMC like 30 Doradus pop up in the map. All over the LMC the average extinction is small and its value in the K_s band is $A_{K_s} = 0.03$ mag with $\sigma = 0.02$ mag. A comparison of the reddening values derived from RC stars (Tatton et al. 2013) and the values estimated from RRLs using the Piersimoni et al. (2002) formula shows that there is a qualitative agreement between the two methods. However, this agreement should be taken with some caution as Tatton et al. (2013)'s work is based on stars in a limited area of the LMC, surrounding the 30 Doradus region. Indeed, substantial differences between the reddening maps derived from RCs, background galaxies, and RRLs were found for example in the SMC by Bell et al. (2020). These differences most likely arise from RCs, RRLs, and background galaxies sampling regions at different depths. In fact, RCs are expected to be embedded in the dust

Downloaded from https://academic.oup.com/mnras/article/504/1/1/6206842 by INAF Capodimonte Napoli (Osservatorio Astronomico di Capodimonte (Napoli) user on 23 March 2022

Table 3. List of LMC RRLs analysed in the paper: OGLE IV ID (five digit number −OGLE-LMC-RRLYR-) or *Gaia* DR2 ID (>9 digit number) column (1), VMC ID is column (2), J2000 coordinates RA and Dec. from the VMC catalogue are columns (3) and (4), pulsation mode (column 5), period (column 6), and epoch of maximum light (−2456000 for OGLE sources, −2455197.5 for *Gaia* DR2 sources) column (7), metallicity is column (8), absorption in the K_s band (column 9), number of epochs in the K_s band (column 10), Y (column 11) and J band (column 12), columns (13), (14), and (15) are average VMC magnitudes: $\langle Y \rangle$, $\langle J \rangle$, and $\langle K_s \rangle$. The table is published in its entirety as Supporting Information with the electronic version of the article. A portion is shown here for guidance regarding its form and content.

ID	ID(VMC)	RA deg	Dec. deg	Type	P (d)	T_0 (d)	[Fe/H] dex	A_{K_s} (mag)	N_{K_s}	N_Y	N_J	$\langle K_s \rangle$ (mag)	$\langle Y \rangle$ (mag)	$\langle J \rangle$ (mag)
34314	558346514686	84.202208	–74.490389	ab	0.7040914	0.46883		0.028	26	8	8	18.12	18.64	18.50
33596	558346517950	82.979042	–74.501333	ab	0.6610381	0.29199	− 1.424	0.035	13	4	4	17.94	18.39	18.21
35139	558346518034	85.807625	–74.498722	ab	0.4889976	0.25714	− 1.592	0.036	13	4	4	18.20	18.88	18.66
34860	558346519807	85.190208	–74.510083	c	0.3114614	0.24308	− 1.507	0.082	13	4	4	18.45	18.88	18.77
34267	558346526561	84.127458	–74.540444	ab	0.53476	0.08816		0.037	13	4	4	18.10	18.53	18.32
34756	558346526744	85.008125	–74.538944	ab	0.55045	0.16538		0.082	12	3	4	17.95	18.37	18.25
34635	558346527385	84.747875	–74.543194	c	0.34962	0.01419	− 1.527	0.043	13	4	4	18.41	18.82	18.60

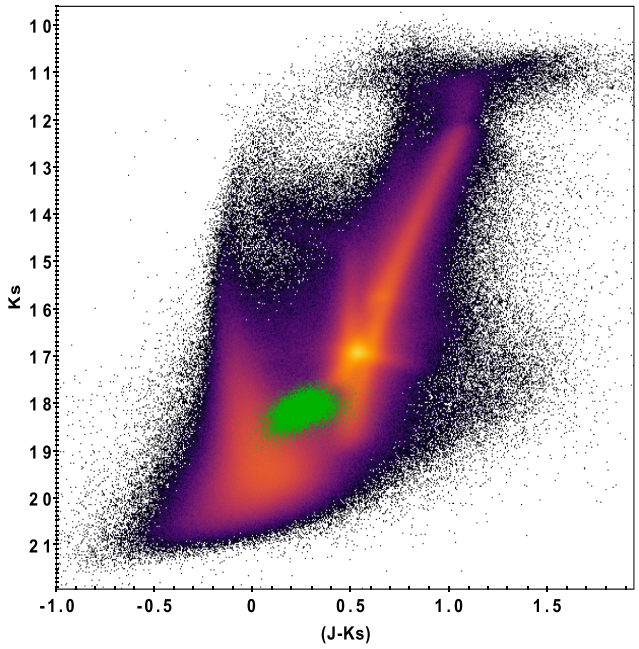

Figure 3. CMD of all VMC sources matching the *Gaia* eDR3 catalogue using the criteria defined in the text. A total of 6.9 million sources are shown in this diagram. The RRLs analysed in this paper are marked by small green dots.

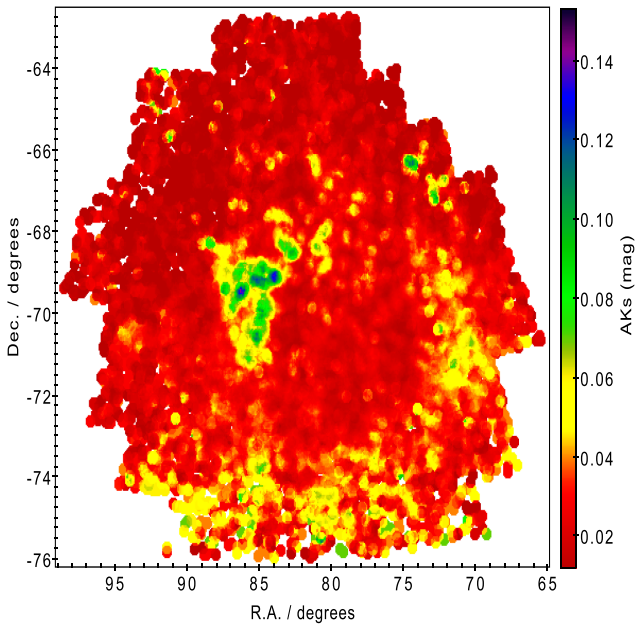

Figure 4. K_s-band absorption map derived from the RRab stars. The position of each RRL was re-binned to a circle of 30 arcsec in diameter.

layers, RRLs probably are half in front and half in the background, and galaxies are definitely in the far field. One can thus expect some spatial correlations in the mean extinction values, but not identical values from these different indicators.

3.3 Blended sources

Our first attempt to derive the PL_{K_s} relation has revealed a number of RRLs brighter than the main relation. We investigated their spatial distribution and found that they are mainly located in the central part of the LMC. This is shown in Fig. 5 which presents in the bottom panel the spatial distribution of the whole sample of RRLs considered in this paper (∼29 000), in the top panel the distribution of the RRLs which appear to be overluminous in the PL_{K_s} relation, and, in the middle panel, the distribution of the RRLs which were actually used to fit our final PL_{K_s} relation. Further investigations, performed using the Fourier parameters (ϕ_{31}, ϕ_{21}, R_{21}, and R_{31}) of the light curves available in the OGLE IV catalogue did not show any particular properties of the overluminous RRLs. On the other hand, in the period–amplitude diagram based on the I amplitudes available in the OGLE IV catalogue, the bright RRLs all show small, in some cases near-zero amplitudes, compared with regular RRLs of the same period. The decrease in amplitude at a given period can be owing to these RRLs being blended with non-variable stars. We expect the centroid of a blended source to be determined with poor accuracy (see e.g. Ripepi et al. 2014, 2015). For this reason as a further test we plotted the distribution of distances in arcsec of the VMC sources cross-matched with the OGLE IV RRLs. A clear separation is now seen in the two samples, for 94 per cent of the RRLs lying on the *PL*/*PW* relations the cross-match radius is less than 0.2 arcsec, whereas for 68 per cent of the overluminous RRLs the cross-match radius is larger than 0.2 arcsec. The average accuracy of the VMC astrometry is of the order of 0.080 arcsec both in RA and in Dec. (Cioni et al. 2011). We therefore discarded the RRLs with a cross-match radius larger than 0.2 arcsec. A total of 3252 objects were discarded. This procedure allowed us to significantly

Downloaded from https://academic.oup.com/mnras/article/504/1/1/6206842 by INAF Capodimonte Napoli (Osservatorio Astronomico di Capodimonte (Napoli) user on 23 March 2022

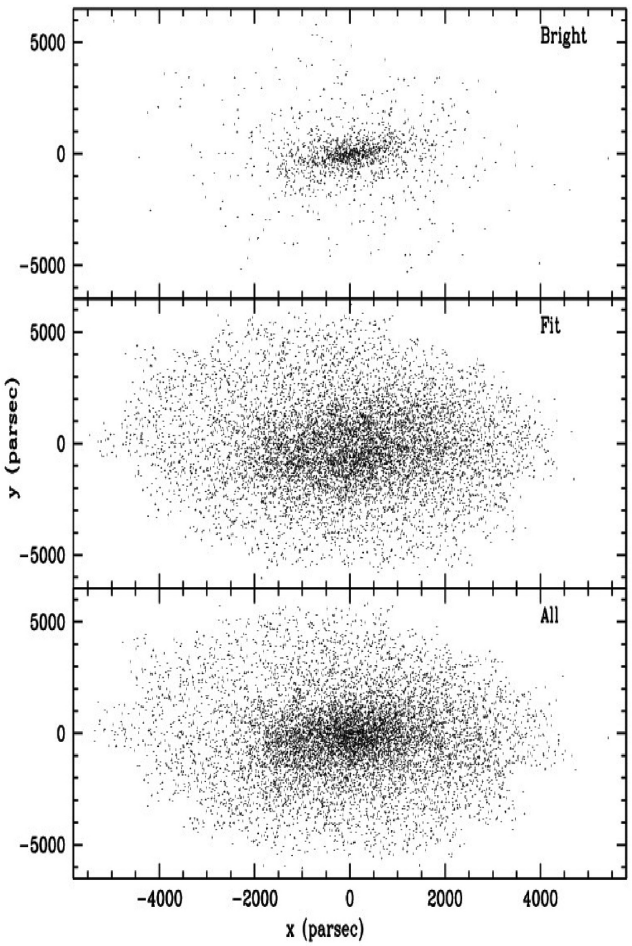

Figure 5. *Bottom:* Spatial distribution of the whole sample of RRLs (∼29 000) considered in the paper; *Middle:* distribution of the RRLs which were actually used to fit the PL_{K_s} relation (∼22 000); *Top:* distribution of the RRLs which appear to be overluminous in the PL_{K_s} relation (∼7000), hence were discarded. They are mainly located along the LMC bar, thus explaining the gap seen in that region in the middle panel.

reduce the scatter on the *PL*/*PW* relations. We visually inspected the VMC images of some of the discarded RRLs, confirming that they all are clearly blended with stars and/or background galaxies. Similar investigations were performed in the past and the same effects were noted, e.g. by Ripepi et al. (2015) for Type II Cepheids. The final sample of LMC RRLs after this cleaning procedure contains 25 795 objects. This is the sample that was used as a starting point to investigate the *PL* and *PW* relations presented in the following sections. Additional RRLs were later discarded from the final fit based on a 3σ clipping procedure leading to PL_{K_s} relations using a clean sample of ∼22 000 RRLs.

3.4 Metallicity of the RRLs

Knowledge of the metallicity (*Z*) is needed to construct *PLZ* and *PWZ* relations for RRLs. However, spectroscopic metallicities are available only for a very limited number of LMC RRLs (e.g. Gratton et al. 2004; Borissova et al. 2004, 2006 and references therein). Jurcsik & Kovács (1996) and Morgan, Wahl & Wieckhorst (2007) showed that it is possible to derive a 'photometric' estimate of the metal abundance ([Fe/H]) of an RRL of known pulsation period from the ϕ_{31} Fourier parameter of the *V*-band light curve decomposition. A new calibration of the ϕ_{31}–[Fe/H] relation for fundamental-mode and first-overtone RRLs was published by Nemec et al. (2013), based on excellent accuracy RRL light curves obtained with the *Kepler* space telescope, and metallicities derived from high-resolution spectroscopy. This new calibration provides metal abundances directly tied to the metallicity scale of Carretta et al. (2009) which is based on high-dispersion spectroscopy and holds for the metallicity range from [Fe/H] ∼ 0.0 to ∼−2.6 dex.

Skowron et al. (2016) applied the calibration of Nemec et al. (2013) to the OGLE-IV fundamental mode RRLs, obtaining a median metallicity value of [Fe/H] = −1.59 ± 0.31 dex for the LMC on the Zinn & West (1984) scale. Metallicities from Skowron et al. (2016) are available for 16 570 LMC RRab stars in our sample. This sample was used to compute a metallicity map of the LMC. Through the interpolation of this map it was possible to give a metallicity estimate also to the RRc stars. The single [Fe/H] values in Skowron et al. (2016) and the ones derived from the metallicity map were used to compute the metallicity-dependent relations listed in Tables 4 and 5. A non-linear least-squares Marquardt–Levenberg algorithm (e.g. Mighell 1999) was used to fit the *PLZ* and *PWZ* relations along with a 3σ clipping procedure to clean from outliers. Our final *PLZ* and *PWZ* relations are based on a sample ∼13 000 RRab and ∼5000 RRc stars (see Tables 4 and 5).

3.5 Derivation of the *PL*(*Z*) and *PW*(*Z*) relations

PL_{K_s}(Z) relations were computed using the periods, $\langle K_s \rangle$ mean magnitudes, absorption values, and metallicity for the RRLs listed in Table 3. We fitted a linear least-squares relation of the form: $m_{X0} = a + b \times \log P + c \times$[Fe/H]. For the global relation (Glob), which includes RRab plus RRc stars, the periods of the RRc stars were fundamentalized using the classical relation $\log P_{FU}(\mathrm{RRc}) = \log P_{\mathrm{RRc}} + 0.127$ (Iben 1974). Only stars with $E(V - I) > 0$ mag were considered and an unweighted least-squares fit with 3σ clipping was applied, hence reducing the sample of RRLs actually used to construct the *PL* relations to around 22 100 sources (∼16 900 RRab and ∼5200 RRc). The same procedure was used to obtain *PL* relations in the *Y* and *J* bands. There are on average only three to four phase points for each RRL in the VMC data available in the *Y* and *J* bands (see Table 2). Hence, the resulting average magnitudes have larger errors and the *PL* relations in *Y* and *J* have larger rms values than for the K_s band. In the optical we obtained a *PL* relation in the *I* band using the OGLE IV data. The *PL* and *PLZ* relations derived using this procedure are summarized in Table 4. In the case of the PL_{K_s} we also derived individual relations for each VMC tile and their parameters are given in Table 1. Fig. 6 shows the *PL* relations in the *I*, *Y*, *J*, and K_s bands obtained for RRab (FU), RRc (FO) on the left and for RRab plus fundamentalized RRc stars (Glob) on the right.

Reddening-independent *PW* relations can be obtained by combining magnitudes and colours in different bands. These reddening free magnitudes were introduced by Madore & van den Bergh (1975) and Madore (1982). They are defined as: $W(X, Y) = m_X - R(m_Y - m_X)$ where *X* and *Y* are two different passbands and *R* is the ratio between selective absorption in the *X* band and colour excess in the adopted colour. These coefficients are fixed according to the Cardelli et al. (1989) law. A set of *PW* and *PWZ* relations was obtained fitting the VMC *Y*, *J*, and K_s and OGLE IV *V*, *I* photometry to the equation $m_X - R \times (m_Y - m_X) = a + b \times \log P + c \times$[Fe/H]. The parameters obtained are summarized in Table 5. The PW relations in different bands are presented in Fig. 7.

Downloaded from https://academic.oup.com/mnras/article/504/1/1/6206842 by INAF Capodimonte Napoli (Osservatorio Astronomico di Capodimonte (Napoli) user on 23 March 2022

Table 4. Parameters of the *PL* and *PLZ* relations in different passbands. The coefficients are for the fits in the form: $m_{X0} = a + b \times \log P + c \times$[Fe/H].

Mode	Band	a	σ_a	b	σ_b	c	σ_c	rms	$N_{\rm star}$
FU	K_{s0}	17.360	0.005	−2.84	0.02			0.14	16 897
FO	K_{s0}	16.860	0.023	−2.98	0.05			0.17	5236
Glob	K_{s0}	17.430	0.004	−2.53	0.01			0.15	22 122
FU	K_{s0}	17.547	0.008	−2.80	0.02	0.114	0.004	0.13	13 081
FO	K_{s0}	16.850	0.026	−2.99	0.05	0.011	0.012	0.17	5132
Glob	K_{s0}	17.603	0.007	−2.41	0.01	0.096	0.004	0.15	17 698
FU	J_0	17.699	0.005	−2.50	0.02			0.15	16 868
FO	J_0	17.241	0.022	−2.53	0.04			0.17	5225
Glob	J_0	17.800	0.004	−2.00	0.01			0.16	22 087
FU	J_0	17.888	0.008	−2.45	0.02	0.121	0.004	0.14	13 081
FO	J_0	17.225	0.030	−2.53	0.05	−0.010	0.012	0.17	4946
Glob	J_0	17.962	0.007	−1.91	0.01	0.095	0.004	0.15	17 757
FU	Y_0	17.990	0.006	−2.25	0.02			0.17	16 866
FO	Y_0	17.550	0.025	−2.26	0.05			0.20	5211
Glob	Y_0	18.110	0.046	−1.66	0.02			0.18	22 071
FU	Y_0	18.207	0.009	−2.18	0.03	0.135	0.005	0.16	13 081
FO	Y_0	17.553	0.033	−2.27	0.05	0.003	0.014	0.19	4946
Glob	Y_0	18.297	0.008	−1.55	0.02	0.108	0.004	0.17	17 783
FU	I_0	18.220	0.005	−2.06	0.02			0.13	16 696
FO	I_0	17.830	0.023	−1.99	0.05			0.18	5142
Glob	I_0	18.350	0.004	−1.42	0.01			0.15	21 838
FU	I_0	18.439	0.006	−1.98	0.02	0.136	0.003	0.11	13 081
FO	I_0	18.439	0.006	−1.98	0.02	0.136	0.003	0.11	13 081
Glob	I_0	18.521	0.006	−1.36	0.01	0.106	0.003	0.13	17 757

3.6 *Gaia* proper motions for the LMC RRLs

The recently released *Gaia* eDR3 catalogue (Gaia Collaboration 2020) includes proper motions for 21 801 RRLs in our catalogue, with average errors of $\sigma_{\mu^*_\alpha} \sim 0.30$ and $\sigma_{\mu_\delta} \sim 0.32$ mas yr^{-1}, respectively. We selected RRL stars in the LMC retaining only sources with proper motions within 1σ from the average proper motions in RA and Dec. of the whole sample of 21 801 RRLs, which are $\langle\mu^*_\alpha\rangle = 1.85$ and $\langle\mu_\delta\rangle = 0.36$ mas yr^{-1}, respectively. This resulted in a subsample of 4690 RRLs. A fit of the PL$_{Ks}$ relation using only this *Gaia* proper motion-selected sample of RRLs provides: $a = 17.44$ mag, $b = -2.55$ mag, $\sigma_a = 0.01$ mag, $\sigma_b = 0.03$ mag, and rms $= 0.14$. This is consistent with the global relation (Glob) presented in Table 4. A similar analysis was performed for the other PL(Z) and PW(Z) relations presented in Tables 4 and 5 obtaining always consistent results. This gives us confidence that the *PL* and *PW* relations derived in this paper are based on samples of RRLs which are bona fide LMC members.

3.7 Comparison with theory and other papers

As a final step of our analysis of the RRL *PL* relations we have compared the *PLZ* and *PWZ* relations obtained here with the theoretical results of Marconi et al. (2015).

Three of our *PLZ* and six of our *PWZ* relations have a counterpart in Marconi et al. (2015). A comparison of the matching relations shows that the slopes in period and metallicity are different, with an average difference of 0.53(±0.05) dex units in the log P term and 0.07(±0.01) dex units in the metallicity term. This is clearly seen in Fig. 8 where the parameters of some PWZ relations derived in this work are compared with those in the corresponding relations by Marconi et al. (2015).

These differences most likely arise from the larger dependence on metallicity of the theoretical relations, which predict metallicity terms of the order of 0.2 mag dex^{-1}. Further comparisons with the theoretical pulsation scenario will be discussed in a future paper (M. I. Moretti et al., in preparation). Such a large metallicity dependence is not observed for several empirical RRL *PLZ* relations in the literature (e.g. Del Principe et al. 2006; Sollima et al. 2008; Borissova et al. 2009). However, using literature data for Milky Way (MW) field RRLs, Muraveva et al. (2018a) derived an empirical absolute *PLZ*(*K*) relation calibrated using *Gaia* DR2 parallaxes, which shows a non-negligible dependence on metallicity, in the same direction as that found by the theoretical *PLZ* relations. Similarly, Sesar et al. (2017b) and then Neeley et al. (2019) using *Gaia* DR2 parallaxes found for the metallicity slopes of the PLZ relations values between 0.17 and 0.20 mag dex^{-1}. A possible explanation for the differences in the metallicity term (and, in turn, also for the log P term) is that the RRLs considered by the Marconi et al. (2015), Muraveva et al. (2018a), Neeley et al. (2019), and Sesar et al. (2017b) span a range in metallicity from $Z = 0.0001$ to $Z = 0.02$, while the metallicity of the LMC RRLs covers a much smaller range from $Z = 0.0001$ to $Z = 0.001$ (Carrera et al. 2008), hence lacking the more metal-rich component observed in the MW. A comparison between the coefficients of the PLZ relations for RRab + fundamentalized RRc stars derived in this paper and in those cited above is shown in Fig. 9. The fit parameters differences range from an almost consistency in 1σ in the J band b parameters to a 6σ difference for c parameters in the same band. Consistently larger differences arise in the Y, J, and K_s bands for the c parameters. While

Downloaded from https://academic.oup.com/mnras/article/504/1/1/6206842 by INAF Capodimonte Napoli (Osservatorio Astronomico di Capodimonte (Napoli) user on 23 March 2022

Table 5. Parameters of the *PW* and *PWZ* relations in different passbands. The parameters are for the fits given in the form: $m_X - R \times (m_Y - m_X) = a + b \times \log P + c \times$[Fe/H].

Mode	Band	R	a	σ_a	b	σ_b	c	σ_c	rms	$N_{\rm star}$
FU	$K_s, J-K_s$	0.69	17.150	0.006	−3.075	0.025			0.17	16 911
FO	$K_s, J-K_s$	0.69	16.600	0.055	−3.289	0.027			0.21	5274
Glob	$K_s, J-K_s$	0.69	17.190	0.004	−2.888	0.016			0.18	22 185
FU	K_s, J-K_s	0.69	17.330	0.009	−3.033	0.027	0.111	0.004	0.16	13 081
FO	K_s, J-K_s	0.69	16.619	0.033	−3.280	0.052	0.008	0.013	0.19	4945
Glob	K_s, J-K_s	0.69	17.348	0.008	−2.810	0.016	0.094	0.004	0.17	17 670
FU	$K_s, Y-K_s$	0.42	17.110	0.006	−3.086	0.024			0.16	16 911
FO	$K_s, Y-K_s$	0.42	16.580	0.026	−3.276	0.053			0.20	5274
Glob	$K_s, Y-K_s$	0.42	17.150	0.004	−2.888	0.015			0.17	22 185
FU	$K_s, Y-K_s$	0.42	17.298	0.009	−3.049	0.026	0.107	0.004	0.15	13 081
FO	$K_s, Y-K_s$	0.42	16.591	0.031	−3.270	0.050	0.008	0.013	0.18	4946
Glob	$K_s, Y-K_s$	0.42	17.306	0.007	−2.813	0.016	0.088	0.004	0.16	17 757
FU	K_s, I-K_s	0.25	17.160	0.006	−3.036	0.023			0.16	16 686
FO	K_s, I-K_s	0.25	16.610	0.026	−3.243	0.052			0.20	5142
Glob	K_s, I-K_s	0.25	17.210	0.004	−2.800	0.015			0.17	21 543
FU	K_s, I-K_s	0.25	17.337	0.009	−2.999	0.027	0.110	0.004	0.15	13 081
FO	K_s, I-K_s	0.25	16.629	0.033	−3.217	0.052	0.004	0.013	0.19	4937
Glob	K_s, I-K_s	0.25	17.368	0.008	−2.711	0.016	0.091	0.004	0.16	17 567
FU	$K_s, V-K_s$	0.13	17.170	0.005	−3.021	0.022			0.15	16 686
FO	$K_s, V-K_s$	0.13	16.630	0.024	−3.216	0.048			0.18	5142
Glob	$K_s, V-K_s$	0.13	17.220	0.004	−2.787	0.014			0.16	21 828
FU	$K_s, V-K_s$	0.13	17.349	0.008	−2.985	0.025	0.109	0.004	0.14	13 081
FO	$K_s, V-K_s$	0.13	16.650	0.031	−3.193	0.049	0.004	0.013	0.18	4957
Glob	$K_s, V-K_s$	0.13	17.380	0.007	−2.701	0.015	0.090	0.004	0.15	17 230
FU	$J, I-J$	0.96	17.190	0.008	−2.921	0.035			0.23	16 686
FO	$J, I-J$	0.96	16.660	0.033	−3.056	0.066			0.25	5142
Glob	$J, I-J$	0.96	17.270	0.006	−2.549	0.022			0.24	21 828
FU	$J, I-J$	0.96	17.358	0.014	−2.903	0.041	0.106	0.007	0.23	13 081
FO	$J, I-J$	0.96	16.658	0.043	−3.040	0.068	−0.007	0.017	0.25	13 081
Glob	$J, I-J$	0.96	17.425	0.011	−2.431	0.023	0.085	0.006	0.23	17 757
FU	$J, V-J$	0.40	17.220	0.006	−2.920	0.027			0.18	16 686
FO	$J, V-J$	0.40	16.700	0.025	−3.038	0.051			0.20	5142
Glob	$J, V-J$	0.40	17.280	0.005	−2.593	0.017			0.18	21 828
FU	$J, V-J$	0.40	17.377	0.010	−2.897	0.031	0.103	0.005	0.17	13 081
FO	$J, V-J$	0.40	16.697	0.033	−3.027	0.052	−0.007	0.013	0.20	4946
FU	$J, V-J$	0.40	17.433	0.009	−2.493	0.017	0.084	0.005	0.18	17 546
FU	$I, V-I$	1.55	17.160	0.004	−3.016	0.018			0.12	16 686
FO	$I, V-I$	1.55	16.690	0.018	−3.101	0.037			0.14	5142
Glob	$I, V-I$	1.55	17.190	0.003	−2.843	0.011			0.13	21 828
FU	$I, V-I$	1.55	17.299	0.006	−2.994	0.019	0.090	0.003	0.11	13 081
FO	$I, V-I$	1.55	16.712	0.024	−3.105	0.037	0.018	0.010	0.11	4954
Glob	$I, V-I$	1.55	17.323	0.006	−2.790	0.012	0.076	0.003	0.12	17 456

for the b parameters the largest difference are seen especially for the K_s band.

4 STRUCTURE OF THE LMC

4.1 Individual distances to RRLs

The *PL* and *PW* relations derived in the previous sections can be used to infer the distance to each RRL in our LMC sample once a zero-point is adopted. For this analysis we do not rely on the PLZ relations as they are based on a smaller sample than the PL relationships. We assumed as distance to the LMC centre the estimate of Pietrzyński et al. (2013) which corresponds to $d_0 = 49.97 \pm 1.12$ kpc or to a distance modulus of $(m - M)_0 = 18.49$ mag. However, this choice does not affect our study of the LMC's structure, for which we rely on differential distances.

We measured the distance to each RRL using the PL_{K_s} relation and two different versions of the *PWZ*s. Results obtained from the three different relations were then compared. Since the *PWZ*s include a metallicity term, their application is limited to the RRab and RRc sample for which we have metallicities. We chose to adopt the $K_s, J-K_s$ and the $K_s, V-K_s$ *PWZ* relations. We adopted the former because

Downloaded from https://academic.oup.com/mnras/article/504/1/1/6206842 by INAF Capodimonte Napoli (Osservatorio Astronomico di Capodimonte (Napoli) user on 23 March 2022

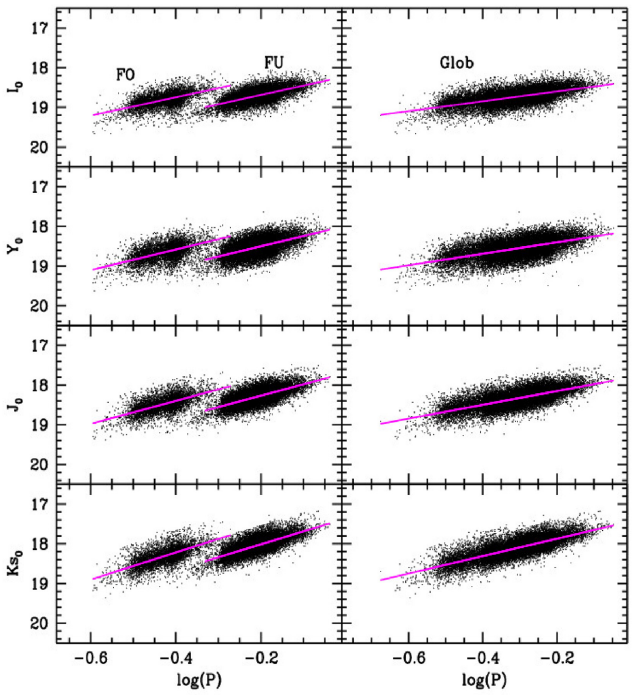

Figure 6. De-reddened mean magnitudes versus log P, for RRLs in the LMC. The black points are stars retained for the final PL computation. The left-hand panels show RRc (first overtone, FO) and RRab stars (fundamental mode, FU) separately. The right-hand panels show all RRLs after the log P of the RRc stars was fundamentalized. The magenta lines show the PL relations derived using these data (see Table 4).

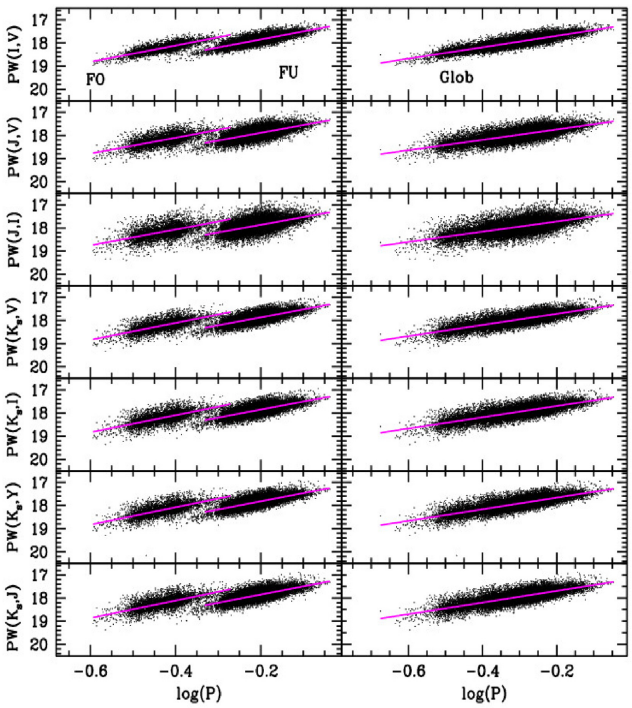

Figure 7. As in Fig. 6 but for Wesenheit magnitudes. The magenta lines show the PW relations presented in Table 5.

the K_s and J bands are less sensitive to possible deviations from the colour correction, and the latter because it is weakly dependent on the colour term ($R = 0.13$). We opted for the PL_{K_s} relation because it is less affected by reddening, and used the global version, which allowed us to determine the distances to 22 122 RRLs of both RRab and RRc types. The average error in the distance estimate for each RRL is of the order of ∼3.5 kpc (∼0.15 mag). The mean difference between the distances measured using the two PWZ relations is 0.45 pc, whereas the mean difference between distances from the $PW(K_s, V - K_s)$ and the PL_{K_s} relations is 23 pc (∼0.001 mag), which is very small compared with the average individual error of each RRL. In the following analysis, we rely on the distances derived using the PL_{K_s} since it is based on a larger sample of RRLs, it has the smaller rms between the PL relations derived here, and the K_s band is the one that is less affected by reddening.

4.2 3D geometry of the LMC

Once the distance to each RRL is determined, it is possible to derive the Cartesian distribution of the RRLs from the RA, Dec. coordinates and the individual distances using the method described by van der Marel & Cioni (2001) and Weinberg & Nikolaev (2001):

$$\begin{aligned} x &= -d\ \sin(\alpha - \alpha_0)\cos\delta \\ y &= d\ \sin\delta\cos\delta_0 - d\ \sin\delta_0\cos(\alpha - \alpha_0)\cos\delta \\ z &= d_0 - d\ \sin\delta\sin\delta_0 - d\ \cos\delta_0\cos(\alpha - \alpha_0)\cos\delta, \end{aligned} \tag{3}$$

where d is the individual distance to each RRL, d_0 is the distance to the LMC centre, and (α_0, δ_0) are the RA and Dec. coordinates of the LMC centre. We assume as reference system (x, y, z) one that has the origin in the LMC centre at (α_0, δ_0, and d_0), the x-axis antiparallel to the RA-axis, the y-axis parallel to the Dec. axis, and the z-axis pointing towards the observer. The α_0, δ_0 coordinates of the LMC centre were derived from the average position of the RRLs ($\alpha_0 = 80^\circ.6147$, $\delta_0 = -69^\circ.5799$). Our centre is offset by ∼0.8° from the LMC centre of El Youssoufi et al. (2019, $\alpha_0 = 81^\circ.24$, $\delta_0 = -69^\circ.73$), which was obtained using stellar density maps of all the stellar populations in the LMC.

As a first approach we divided the LMC into (x, y) planes by considering different intervals in distance. Fig. 10 shows the distribution of the LMC RRLs in Cartesian coordinates divided into bins of distance. The bins were of the same order as the average distance standard deviation, ∼3.5 kpc. Going clockwise from the top right-hand panel the RRLs are mapped for increasing distance values. A quick look shows that there are two extreme cases, with the RRLs closest (top right-hand panel) and most distant to us (top left-hand panel) showing different spatial distributions. A fraction of the RRLs in the top right-hand panel of Fig. 10 appears to be spread all over the field and are likely RRLs belonging to the MW halo. This view is corroborated by the proper motions of the RRLs in this sample of which 43 per cent are outside of 1σ the average μ^*_α and μ_δ values. These stars are placed mainly in the central region of this plot. On the other hand, it is also possible that this sample of RRLs belong to the outermost region of the elongated LMC halo, which is distorted by tidal forces owing to the interaction with the MW. This would explain why the proper motions are different from the average values in the main body of the LMC. In the same direction El Youssoufi et al. (submitted, see section 2.3) find that the centre of the stellar proper motions for stars in the outer regions of the SMC is shifted from that of the inner regions, suggesting that these stars are probably associated with the LMC. In the same sample a concentration of RRLs likely belonging to the LMC shows up right

Downloaded from https://academic.oup.com/mnras/article/504/1/1/6206842 by INAF Capodimonte Napoli (Osservatorio Astronomico di Capodimonte (Napoli) user on 23 March 2022

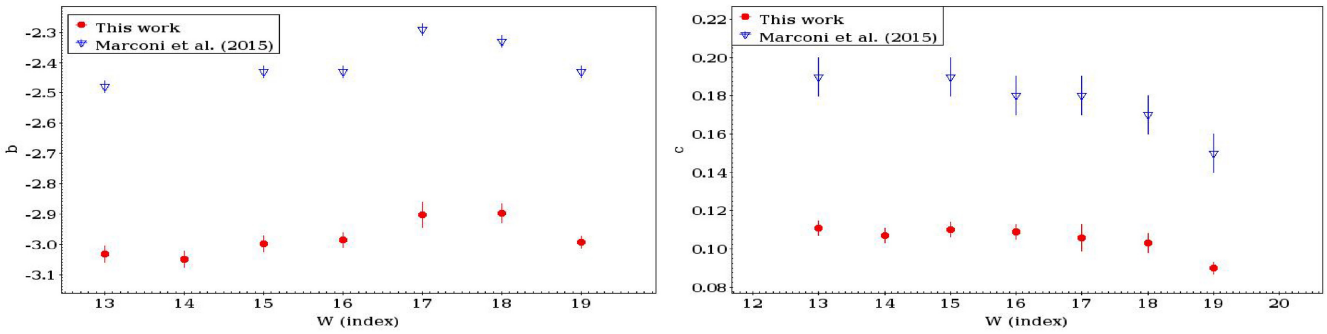

Figure 8. Comparison of the coefficients of the PWZ relations for RRab stars derived in this paper with those of the corresponding relations of Marconi et al. (2015). In the left-hand panel are shown the period slopes, while the right-hand panel shows the metallicty slopes. The W indices are labelled as follows: 13 = $PW(K_s, J)$, 14 = $PW(K_s, Y)$, 15 = $PW(K_s, I)$, 16 = $PW(K_s, V)$, 17 = $PW(J, I)$, 18 = $PW(J, V)$, and 19 = $PW(I, V)$.

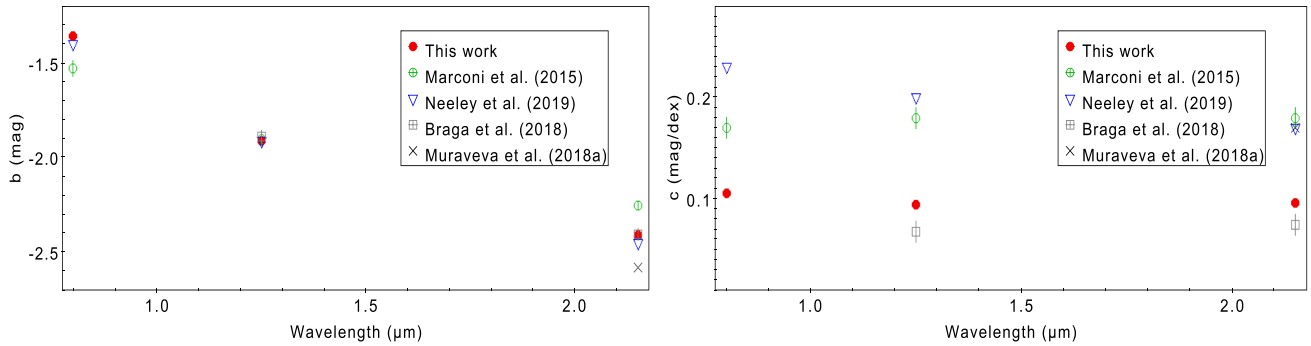

Figure 9. Comparison of the coefficients of the PLZ relations for RRab + fundamentalized RRc stars derived in this paper with those indicated in the legend. The period slopes are shown in the left-hand panel and the metallicity slopes in the right-hand panel. The errors of Neeley et al. (2019) and Muraveva et al. (2018a) are not reported to avoid confusion.

and south of the centre. That is the part of the LMC which points towards the MW. The average coordinates of the RRLs in this panel are $\langle(x, y)\rangle = (-309, 241)$ pc and they represent 5.1 per cent of the whole sample. In the middle right-hand panel are shown RRLs with distances between 44 and 47 kpc and it is still possible to notice a protrusion of stars in the same region as in the previous panel. The centre coordinates in this case are $\langle(x, y)\rangle = (-667, 491)$ pc, for 12.5 per cent of RRLs. Between 47 and 53 kpc (bottom two panels) there are RRLs that belong with good confidence to the LMC and its halo. In the bottom right-hand panel ($47 < d < 50$ kpc) the RRLs are distributed in what is reminiscent of a regular, spherical shape and no particular structures are seen. The centre of the distribution is at $\langle(x, y)\rangle = (-374, 51)$ pc for 31.2 per cent of the RRLs. In the bottom left-hand panel ($50 < d < 53$ kpc) a lack of RRLs along the central part of the LMC bar is visible (see also the middle panel of Fig. 5). This is the region of the highest crowding where many RRLs, although recovered in the VMC catalogue, are found to be located above the *PL* relations owing to contamination by close sources, and which hence were discarded (see Section 3.3). A similar feature was detected using the OGLE IV catalogue by Jacyszyn-Dobrzeniecka et al. (2017), who likewise concluded that it is probably caused by source crowding and blending. The distribution peaks at $\langle(x, y)\rangle = (241, -401)$ pc for 34.1 per cent of the total sample. In the middle left-hand panel there are stars with distances between $53 < d < 56$ kpc, and they represent 12.5 per cent of the total with centre coordinates at $\langle(x, y)\rangle = (435, -343)$ pc. The top left-hand panel shows the most distant RRLs, corresponding to 4.6 per cent of the total sample. Their distribution peaks at $\langle(x, y)\rangle = (338, -234)$ pc. We thus conclude that the LMC has a regular shape similar to an ellipsoid with the north-eastern stars closer to us than the south-western component.

No particular structures other than that of an ellipsoid are seen. To derive the parameters of the ellipsoid we used a similar approach as that used by Deb & Singh (2014) and which is described in section 5.2 of their paper. The three axes of the ellipsoid that we derived are $S_1 = 6.5$ kpc, $S_2 = 4.6$ kpc, and $S_3 = 3.7$ kpc. We found an inclination relative to the plane of the sky and a position angle of the line of nodes (measured from north to east) of $i = 22 \pm 4°$ and $\theta = 167 \pm 7°$, respectively. These results are in agreement with Deb & Singh (2014) who found $i = 24.02°$ and $\theta = 176.01°$. Our result for the inclination also compares well with other papers in the literature: for example, Nikolaev et al. (2004) found $i = 30.7 \pm 1.1°$ using CCs. The small difference in the values can be attributed to the different stellar populations used as RRLs trace old stars which should be more smoothly distributed, while young stars such Cepheids are found in star-forming regions located mainly in the disc of the galaxy.

Combining the results described above we can now visualize the 3D shape of the LMC as traced by its RRLs. This is shown in Fig. 11 for different viewing angles. The overall LMC structure is that of an elongated ellipsoid with a protrusion of stars more distant and closer to us extending from the centre of the LMC. This singular feature, also found by other studies based on OGLE IV RRLs (see e.g. Jacyszyn-Dobrzeniecka et al. 2017), is not a real physical structure and is mainly due to blended sources in the centre of the LMC. However, we cannot completely exclude that the innermost regions, which are at present significantly influenced by crowding, may harbour additional substructures. The regions of the ellipsoid

Downloaded from https://academic.oup.com/mnras/article/504/1/1/6206842 by INAF Capodimonte Napoli (Osservatorio Astronomico di Capodimonte (Napoli) user on 23 March 2022

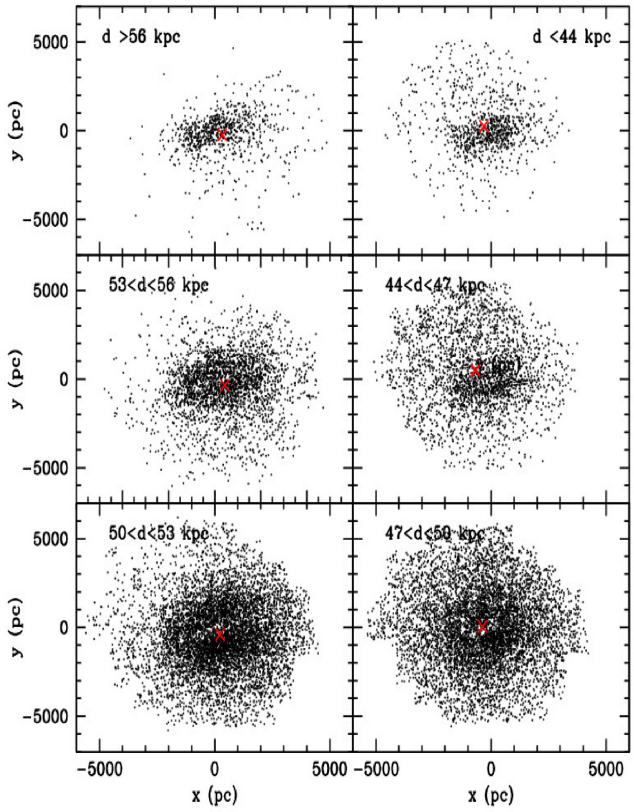

Figure 10. LMC RRLs divided into bins of heliocentric distance, as indicated by the labels. The average centre of the distribution in each panel is marked with a red cross.

extending to the north-eastern direction are closer to us than those in the opposite south-western direction. The difference in heliocentric distance between these two regions is of the order of 2 kpc.

The analysis was repeated by slicing the LMC into bins of metallicity. Results are shown in Fig. 12. We used the metallicities derived by Skowron et al. (2016) for 13 016 RRab stars with a VMC counterpart and for 4742 RRc stars we used the metallicities derived by our LMC metallicity map. No particular structures are seen in Fig. 12, except for the extreme cases of metal-rich ([Fe/H]>-0.5 dex) and metal-poor ([Fe/H] <-2.1 dex) RRLs which appear to be uniformly distributed across the field of view, and which may belong to the MW. Like Deb & Singh (2014) we do not find any metallicity gradient or particular substructures related to large differences in metallicity.

The same procedure was applied to construct a scan map using the proper motions of the LMC RRLs available in *Gaia* eDR3. As described in Section 3.6, the *Gaia* eDR3 catalogue includes proper motions for 21 801 RRLs in our VMC catalogue, with average uncertainties of $\sigma_{\mu^*_\alpha} \sim 0.30$ mas yr^{-1} and $\sigma_{\mu_\delta} \sim 0.32$ mas yr^{-1}. Mean proper motion values for the LMC RRLs are $\mu^*_\alpha = 1.87 \pm 0.54$ mas yr^{-1} and $\mu_\delta = 0.36 \pm 0.80$ mas yr^{-1}, in RA and Dec., respectively. The RRLs scan map we constructed around these values is shown in Fig. 13. Going clockwise from the top right-hand panel the RRLs are mapped by increasing the values in proper motion in the declination coordinate. A gradient of μ_δ with position is clearly seen. The two top panels of Fig. 13 show the extreme cases: the spatial distribution of the RRLs is very different with average positions of $\langle(x, y)\rangle = (-762, -152)$ pc and $\langle(x, y)\rangle = (677, -64)$ pc for $\mu_\delta > 1.4$ mas yr^{-1} and $\mu_\delta < -0.7$ mas yr^{-1}. This is probably owing to the rotation of the LMC as also found by Gaia Collaboration (2018b). We performed a similar analysis using μ^*_α obtaining a less evident gradient, but with a detectable difference between the south-western part and the north-eastern component of $\sim$0.25 mas yr^{-1}.

4.3 GC distances

Although neither OGLE IV nor VMC were designed to resolve stars in clusters given their limited spatial resolution, they detected a number of variable stars also in the LMC star clusters. In order to test the 3D structure of the LMC found in our study, we therefore analysed the RRLs in three LMC GCs, namely, NGC 1835, NGC 2210, and NGC 1786, whose RRLs have been observed by OGLE IV (Soszyński et al. 2016). Those stars are mostly found in the periphery of the GCs in less crowded regions. These three GCs were selected because they are located in different regions of the LMC and observed by the VMC survey (see Fig. 1). For NGC 1835 (the magenta square in Fig. 1), which is located at the western edge of the LMC, there are nine RRLs (four RRab and five RRc pulsators) in common between the OGLE IV catalogue and our VMC RRL sample. We computed a very tight $PW(K_s, J - K_s)$ relation from these RRLs, with a scatter of only 0.10 mag. This confirms that the stars are all at the same distance with similar reddening and metallicity, as expected for a GC. The distance to NGC 1835 we found using the RRL $PW(K_s, J - K_s)$ relation is $d_{\rm NGC1835} = 52.4 \pm 2.3$ kpc. Three of the four RRab stars also have an estimate of the metallicity from Skowron et al. (2016). Their average value is [Fe/H]~-1.84 dex, in agreement with literature values (see e.g. Walker 1993; Olsen et al. 1998). We applied the same procedure to NGC 2210 (the blue circle in Fig. 1) which is located at the eastern edge of the VMC footprint. The $PW(K_s, J - K_s)$ relation, based on eight RRLs in the cluster, is also very tight with a scatter of 0.09 mag which leads to a distance to NGC 2210 of $d_{\rm NGC2210} = 47.6 \pm 2.3$ kpc. Located $\sim$1.5 deg to the north of NGC 1835 the GC NGC 1786 (the green triangle in Fig. 1) has five RRLs in common between the VMC and OGLE catalogues which leads to a *PW* relation with a scatter of only 0.08 mag. The average distance to these stars is $d_{\rm NGC1786} = 49.9 \pm 2.4$ kpc. Although the distances of the three clusters are consistent within 1σ there is a hint that, as found in the previous section, the eastern part of the LMC is closer to us than the western part.

5 DISCUSSION AND CONCLUSIONS

We have obtained new NIR (K_s-, *J*-, and *Y*-band) and optical (*I* band) *PL*, *PW*, *PLZ*, and *PWZ* relations from a sample of $\sim$22 000 RRLs in the LMC using the VMC, OGLE IV, and *Gaia* data sets. Our starting sample comprised more than $\sim$29 000 RRLs with a counterpart in the VMC catalogue. However, about $\sim$7000 RRLs located in the central, very crowded regions of the LMC were discarded using a 3σ clipping procedure and the matching radius criterion, since they were overluminous with respect to the *PL*/*PW* relations. A similar effect was found in the OGLE IV data by Jacyszyn-Dobrzeniecka et al. (2017), who started with an original sample of 27 500 RRab stars and ended up with their final fit being based on a subset of about $\sim$19 500 of them. Our sample of $\sim$22 000 RRLs is the largest sample of RRLs used to date to obtain NIR *PL*s. Previous NIR–PL relations available in the literature were based on limited samples (see e.g. Borissova et al. 2009, based on $\sim$40 RRLs) and small fields of view (e.g. Sollima, Cacciari & Valenti 2006). Moreover, this is the first set of *PLZ* and *PWZ* relations in the *Y*-band for RRLs in the LMC. Future facilities like James Webb Space Telescope (JWST) and The Extremely Large Telescope (ELT) will allow the detection of RRLs

Downloaded from https://academic.oup.com/mnras/article/504/1/1/6206842 by INAF Capodimonte Napoli (Osservatorio Astronomico di Capodimonte (Napoli) user on 23 March 2022

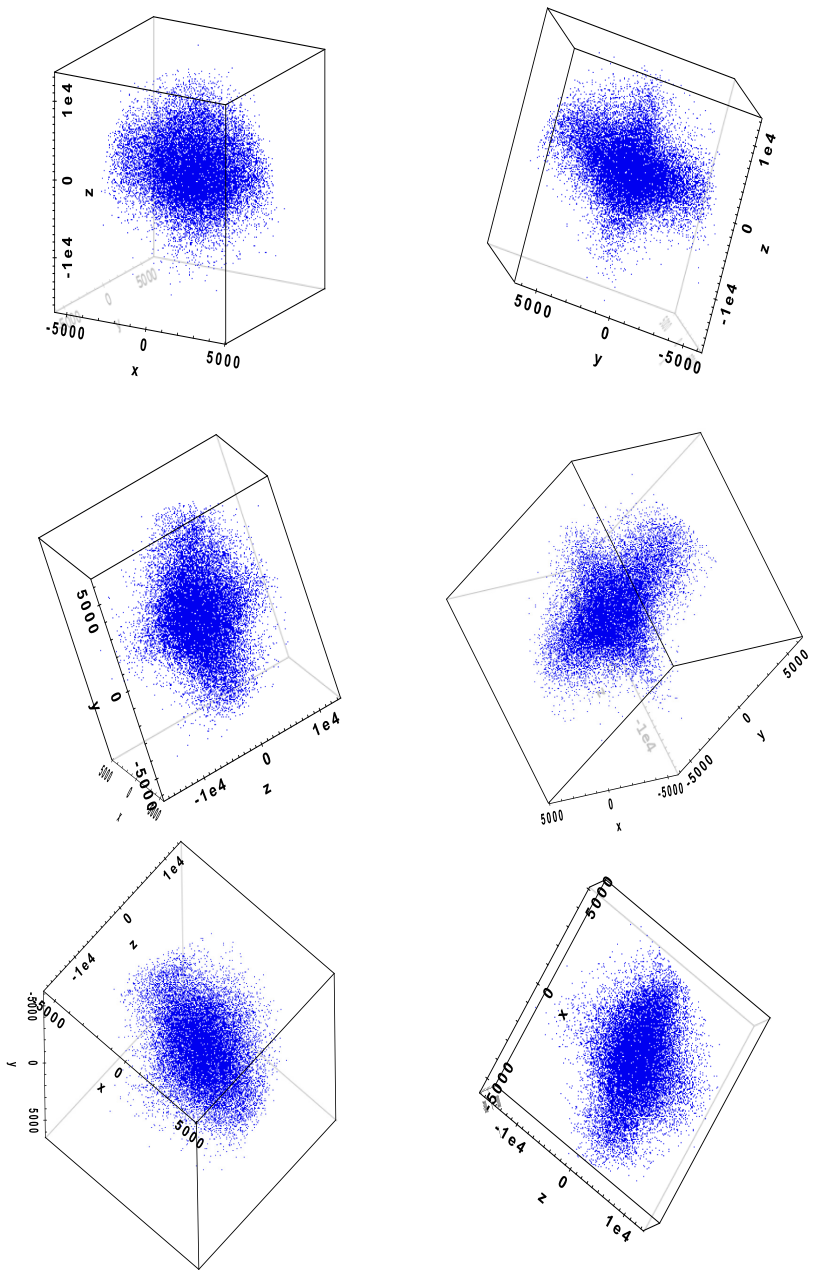

Figure 11. 3D shape of the LMC inferred from the RRLs, as seen from different viewing angles. The protrusion of sources extending from the LMC centre could be due to crowding effects. Units along the axes are parsecs.

in galaxies in the Virgo cluster ∼20 Mpc away from us. The rms of the relations we have obtained is good enough that RRLs with just one phase point on their NIR light curves will be sufficient to get an estimate of distance moduli accurate up to ∼0.15 mag. Along with future observations of RRLs in galaxies outside the Local Group, our relations can thus be used to improve the calibration of the cosmic distance ladder.

The comparison of our *PLZ* relations with the theoretical relations of Marconi et al. (2015) and with observed *PLZ* in the literature (Braga et al. 2018; Muraveva et al. 2018a; Neeley et al. 2019) indicates that the dependence on metallicity is more significant for high metallicities. However, the LMC lacks such metal-rich RRLs, hence biasing the comparison between theoretical and empirical relations.

Applying the relation of Piersimoni et al. (2002) we derived individual reddening estimates for the RRab stars and obtained a reddening map for the whole LMC. This map was used to provide a reddening estimate for all RRLs in our sample.

RA and Dec. coordinates of the LMC centre were derived from the average position of the RRLs and found to be at $\alpha_0 = 80^\circ.6147$, $\delta_0 = -69^\circ.5799$. This agrees within 2° of almost all centre estimates available in the literature (e.g. Nikolaev et al. 2004, based on CCs; van der Marel & Kallivayalil 2014, for other tracers). The same authors also showed that the choice of the centre influences the 3D-shape

Downloaded from https://academic.oup.com/mnras/article/504/1/1/6206842 by INAF Capodimonte Napoli (Osservatorio Astronomico di Capodimonte (Napoli) user on 23 March 2022

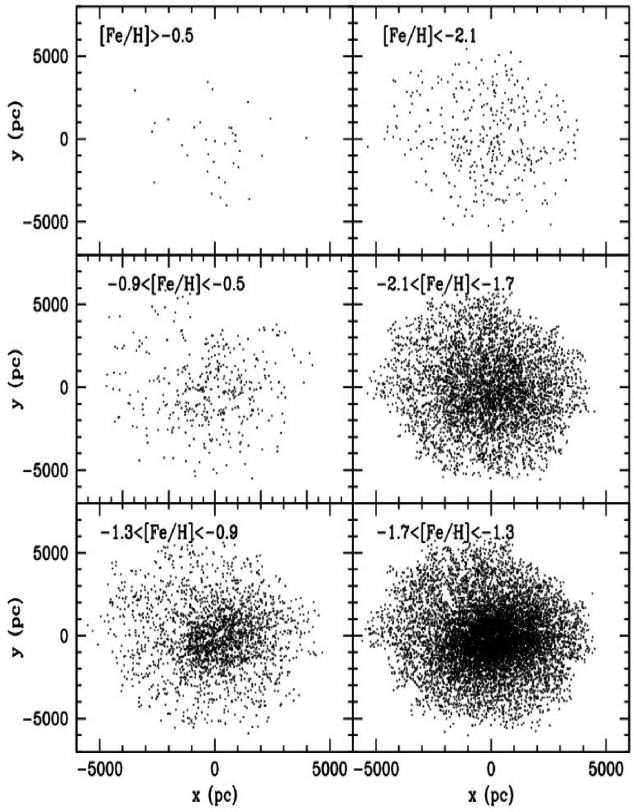

Figure 12. LMC RRLs divided into bins of metallicity, as indicated by the labels.

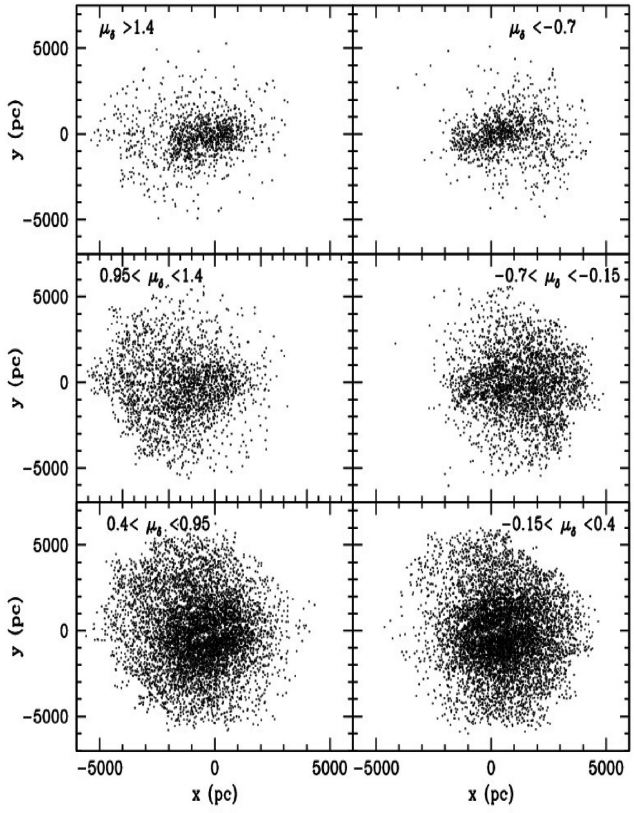

Figure 13. LMC RRLs divided into bins of proper motion in declination, as indicated in the labels.

reconstruction of the LMC, but that differences are rather small and change the determination of the inclination and position angle by only a few degrees.

We used our PL_{K_s} relation to estimate individual distances to ∼22 000 RRLs and from them we reconstructed the 3D structure of the LMC, as traced by these Population II stars. The LMC resembles a regular ellipsoid with an axes ratio of 1:1.2:1.8, where the north-eastern part of the ellipsoid is closer to us. The position angle and orientation of the bar identified by El Youssoufi et al. (2019) (see fig. 5 in their paper) resembles the band devoid of RRLs seen in our Fig. 10 ($50 < d < 53$ kpc panel). A lack of RRLs in this region is likely caused by the significant crowding conditions in the bar, which prevents the determination of good centroids for the RRLs as well as a proper estimate of their magnitudes. Therefore, we did not directly detect the LMC bar using the RRLs, in agreement with a previous study based on OGLE IV data and optical *PW* relations (Jacyszyn-Dobrzeniecka et al. 2017).

A protrusion of stars extending on both sides from the centre of the LMC might be the result of blended sources which are still present in our sample notwithstanding the selection steps we performed. These blended sources are very difficult to eliminate since they mix together in every parameter space. However, it is very unlikely that this structure represents a real streaming of RRLs caused by the SMC/LMC interaction. Besla et al. (2012) presented two models of possible past interactions between the SMC and LMC, of which one is a direct collision. These models allow a good reproduction of different peculiar features of both galaxies, but in neither simulations there is a hint of a stellar component projected from the centre of the LMC along the $|z|$ direction.

Using metallicities from Skowron et al. (2016) for a subsample of ∼13 000 LMC RRab stars and for ∼5000 RRc stars using metal abundances derived from our metallicity map we determined *PLZ* and *PWZ* relations in the VMC (Y, J and K_s) and optical (I) OGLE IV passbands. We also studied the 3D spatial distribution of the RRLs based on their metallicities and we did not detect any metallicity gradient or substructure, confirming previous findings (e.g. Deb & Singh 2014).

Gaia eDR3 proper motions are available for a sample of ∼21 000 RRLs in the VMC catalogue. We used the proper motions to select RRLs which are bona fide members of the LMC and derived a PL_{K_s} which is fully consistent with the relation derived from the full RRL sample. Using the *Gaia* eDR3 proper motions we also detected the rotation of the LMC as traced by its >10 Gyr old stars, in full agreement with Gaia Collaboration (2018b) and Gaia Collaboration (2020c) which used a larger sample (∼8 million) of LMC stars. Some of the RRLs that possess large proper motions, compared with the average value, and are located on the side closer to us, can also be attributed to tidal stream components pointing towards the MW.

ACKNOWLEDGEMENTS

We thank the Cambridge Astronomy Survey Unit (CASU) and the Wide Field Astronomy Unit (WFAU) in Edinburgh for providing calibrated data products under support of the Science and Technology Facility Council (STFC) in the UK. M-RC acknowledges support from the European Research Council (ERC) under European Union's Horizon 2020 research and innovation programme (grant agreement no. 682115). This work makes use of data from the ESA mission *Gaia* (https://www.cosmos.esa.int/gaia), processed by the *Gaia* Data Processing and Analysis Consortium (DPAC, https://www.cosmos.esa.int/web/gaia/dpac/consortium). Funding for the

Downloaded from https://academic.oup.com/mnras/article/504/1/1/6206842 by INAF Capodimonte Napoli (Osservatorio Astronomico di Capodimonte (Napoli) user on 23 March 2022

DPAC has been provided by national institutions, in particular the institutions participating in the *Gaia* Multilateral Agreement.

Based on observations made with VISTA at ESO under programme ID 179.B-2003.

DATA AVAILABILITY

The data underlying this article are available in the article and in its online supplementary material or will be shared on reasonable request to the corresponding author.

REFERENCES

Alcock C. et al., 1997, AJ, 114, 326
Bell C. P. M. et al., 2020, MNRAS, 499, 993
Besla G., Kallivayalil N., Hernquist L., van der Marel R. P., Cox T. J., Kereš D., 2012, MNRAS, 421, 2109
Borissova J., Minniti D., Rejkuba M., Alves D., 2006, A&A, 460, 459
Borissova J., Minniti D., Rejkuba M., Alves D., Cook K. H., Freeman K. C., 2004, A&A, 423, 97
Borissova J., Rejkuba M., Minniti D., Catelan M., Ivanov V. D., 2009, A&A, 502, 505
Braga V. F. et al., 2018, AJ, 155, 137
Cardelli J. A., Clayton G. C., Mathis J. S., 1989, ApJ, 345, 245
Carrera R., Gallart C., Hardy E., Aparacio A., Zinn R., 2008, AJ, 135, 836
Carretta E. et al., 2009, A&A, 505, 117
Cioni M.-R., , Ripepi V., Clementini G., Groeneweg M. A. T , Moretti M. I., Muraveva T. , Subramanian S., 2017, in Catelan M., Gieren W., eds, EPJ Web of Conf., Wide-Field Variability Surveys: A 21st Century Perspective - 22nd Los Alamos Stellar Pulsation - Conference Series Meeting,, , Vol. 152, 01008
Cioni M.-R. L. et al., 2011, A&A, 527, A116
Clementini G. et al., 2000, AJ, 120, 2054
Clementini G. et al., 2019, A&A, 662, A60
Cross N. J. G. , et al., 2012, A&A, 548, A119
Deb S., Singh H. P., 2014, MNRAS, 438, 2440
Del Principe M. et al., 2006, ApJ, 652, 362
Di Criscienzo M. et al., 2011, AJ, 141, 81
El Youssoufi D. et al., 2019, MNRAS, 490, 1076
Gaia Collaboration, 2016a, A&A, 595, A1
Gaia Collaboration, 2016b, A&A, 595, A2
Gaia Collaboration, 2018a, A&A, 616, A1
Gaia Collaboration, 2018b, A&A, 616, A12
Gaia Collaboration, 2020, preprint (arXiv:2012.01771)
Gaia Collaboration, Brown A. G. A., Vallenari A., Prusti T., de Bruijne J. H. J., Babusiaux C., Biermann M., 2020, preprint (arXiv:2012.01533)
González-Fernández C. et al., 2018, MNRAS, 474, 5459
Gratton R. G., Bragaglia A., Clementini G., Carretta E., Di Fabrizio L., Maio M., Taribello E., 2004, A&A, 421, 937
Iben I. Jr, 1974, ARA&A, 12, 215
Jacyszyn-Dobrzeniecka A. M. et al., 2017, Acta Astron., 67, 1
Jurcsik J., Kovacs G., 1996, A&A, 312, 111
Kato D. et al., 2007, PASJ, 59, 615
Kerber L. O., Girardi L., Rubele S., Cioni M.-R. L., 2009, A&A, 499, 697
Lewis J. R., Irwin M., Bunclark P., 2010, ASP Conf. Ser. Vol. 434, Astronomical Data Analysis Software and Systems XIX, Astron. Soc. Pac., San Francisco, p. 91.
Longmore A. J., Fernley J. A., Jameson R. F., 1986, MNRAS, 220, 279
Madore B. F., 1982, ApJ, 253, 575
Madore B. F., van den Bergh S., 1975, ApJ, 197, 55
Marconi M. et al., 2015, ApJ, 808, 50
Mighell K. J., 1999, ApJ, 518, 380
Moretti M. I. et al., 2014, MNRAS, 437, 2702
Moretti M. I. et al., 2016, MNRAS, 459, 1687
Morgan S. M., Wahl J. N., Wieckhorst R. M., 2007, MNRAS, 374, 1421
Muraveva T., Delgado H. E., Clementini G., Sarro L. M., Garofalo A., 2018a, MNRAS, 481, 1195
Muraveva T. et al., 2014, MNRAS, 443, 432
Muraveva T. et al., 2015, ApJ, 807, 127
Muraveva T. et al., 2018b, MNRAS, 473, 3131
Neeley J. R. et al., 2019, MNRAS, 490, 4254
Nemec J. M., Cohen J. G., Ripepi V., Derekas A., Moskalik P., Sesar B., Chadid M., Bruntt H., 2013, ApJ, 773, 181
Nemec J. M., Nemec A. F. L., Lutz T. E., 1994, AJ, 108, 222
Nikolaev S., Drake A. J., Keller S. C., Cook K. H., Dalal N., Griest K., Welch D. L., Kanbur S. M., 2004, ApJ, 601, 260
Olsen K. A. G., Hodge P. W., Mateo M., Olszewski E. W., Schommer R. A., Suntzeff N. B., Walker A.R., 1998, MNRAS, 300, 665
Piersimoni A. M., Bono G., Ripepi V., 2002, AJ, 124, 1528
Pietrzynski G. et al., 2013, Nature, 495, 76
Ripepi V., Moretti M. I., Clementini G., Marconi M., Cioni M.R., Marquette J. B., Tisserand P., 2012a, Ap&SS, 341, 51
Ripepi V. et al., 2012b, MNRAS, 424, 1807
Ripepi V. et al., 2014, MNRAS, 437, 2307
Ripepi V. et al., 2015, MNRAS, 446, 3034
Ripepi V. et al., 2016, ApJS, 224, 21
Ripepi V. et al., 2017, MNRAS, 472, 808
Rubele S. et al., 2012, A&A, 537, A106
Rubele S. et al., 2015, MNRAS, 449, 639
Rubele S. et al., 2018, MNRAS, 478, 5017
Sandage A., 1981a, ApJ, 244, L23
Sandage A., 1981b, ApJ, 248, 161
Sesar B., Fouesneau M., Price-Whelan A. M., Bailer-Jones C. A. L., Gould A., Rix H.-W., 2017b, ApJ, 838, 107
Skowron D. M. et al., 2016, Acta Astron., 66, 269
Skrutskie M. F. et al., 2006, AJ, 131, 1163
Sollima A., Cacciari C., Arkharov A. A. H., Larionov V. M., Gorshanaov D. L., Efimova N. V., Piersimoni A., 2008, MNRAS, 384, 1583
Sollima A., Cacciari C., Valenti E., 2006, MNRAS, 372, 1675
Soszyński I. et al., 2009, Acta Astron., 59, 1
Soszyński I. et al., 2012, Acta Astron., 62, 219
Soszyński I. et al., 2016, Acta Astron., 66, 131
Soszyński I. et al., 2019, Acta Astron., 69, 87
Subramanian S. et al., 2017, MNRAS, 467, 2980
Szewczyk O. et al., 2008, AJ, 136, 272
Tatton B. L. et al., 2013, A&A, 554, A33
Tisserand P. et al., 2007, A&A, 469, 387
Udalski A., Kubiak M., Szymanski M., 1997, Acta Astron., 47, 319
van Albada T. S., Baker N., 1971, ApJ, 169, 311
van den Bergh S., 1993, MNRAS, 262, 588
van der Marel R. P., Cioni M.-R. L., 2001, AJ, 122, 1807
van der Marel R. P., Kallivayalil N., 2014, ApJ, 781, 121
Walker A. R., 1993, AJ, 105, 527
Weinberg M. D., Nikolaev S., 2001, ApJ, 548, 712
Zinn R., West M. J., 1984, ApJS, 55, 45

SUPPORTING INFORMATION

Supplementary data are available at *MNRAS* online.

Table 2. Y, J, and K_s time-series photometry for the RRLs analysed in this paper.
Table 3. List of LMC RRLs analysed in the paper.

Please note: Oxford University Press is not responsible for the content or functionality of any supporting materials supplied by the authors. Any queries (other than missing material) should be directed to the corresponding author for the article.

This paper has been typeset from a TEX/LATEX file prepared by the author.

Downloaded from https://academic.oup.com/mnras/article/504/1/1/6206842 by INAF Capodimonte Napoli (Osservatorio Astronomico di Capodimonte (Napoli) user on 23 March 2022